# Heavy residues from very mass-asymmetric heavy-ion reactions

K. A. Hanold,[1,*] D. Bazin,[2] M. F. Mohar,[2,†] L. G. Moretto,[1] D. J. Morrissey,[2,3] N. A. Orr,[2,‡] B. M. Sherrill,[2,4]
J. A. Winger,[2,§] G. J. Wozniak,[1] and S. J. Yennello[2,//]

[1]*Lawrence Berkeley Laboratory, 1 Cyclotron Road, Berkeley, California 94720*
[2]*National Superconducting Cyclotron Laboratory, Michigan State University, East Lansing, Michigan 48824*
[3]*Department of Chemistry, Michigan State University, East Lansing, Michigan 48824*
[4]*Department of Physics, Michigan State University, East Lansing, Michigan 48824*

The isotopic production cross sections and momenta of all residues with nuclear charge greater than 39 from the reaction of 26, 40, and 50 MeV/nucleon $^{129}$Xe+Be, C, and Al were measured. The isotopic cross sections, the momentum distribution for each isotope, and the cross section as a function of nuclear charge and momentum are presented here. The new cross sections are consistent with previous measurements of the cross sections from similar reaction systems. The results are compared to a geometric incomplete fusion model and a Boltzmann-Nordheim-Vlasov model. Agreement between the models and the data is fair. The most proton-rich nuclei observed in this study are predicted to have less than 50 nb production cross sections by both of these models but are observed to have much larger cross sections.

PACS number(s): 25.70.Gh, 25.70.Jj

## I. INTRODUCTION

The characterization of the source of complex fragments ($Z \geq 3$) in heavy-ion-induced reactions is presently of great interest. Complex fragment (CF) emission has been observed over a wide range of bombarding energies and combinations of projectile and target [1–37]. CF data have been used as a tool to characterize the reaction mechanism of heavy-ion reactions.

For asymmetric entrance channel reactions such as $^{139}$La + C, studies have demonstrated the presence of a single source that emits complex fragments [17,38]. Information about this source was extracted from coincidence measurements of the complex fragments. The observed source velocity ($v_{source}$) was shown to be consistent with complete fusion at low beam energies ($E/A <$ 30 MeV/nucleon) [17,39] and with incomplete fusion at higher beam energies ($E/A >$ 30 MeV/nucleon) [26,36,40]. The center-of-mass angular distributions ($d\sigma/d\theta$) of the complex fragments were isotropic for a range of fragments with masses between the mass of the projectile and that of the target. These isotropic distributions result from the statistical decay of the fused product. The angular distributions of fragments with $Z$ values near those of the projectile and target have both isotropic and anisotropic components. The anisotropic component results from the deep-inelastic process.

In contrast, more symmetric heavy-ion collisions show a more complicated picture. The reaction of $^{139}$La + Ni at 18 MeV/nucleon, for example, produces complex fragment velocity distributions that show no well-defined source [21]. The $v_{source}$ from this reaction ranges from the velocity corresponding to complete fusion to near the velocity of the beam. By gating on the $v_{source}$, it was possible to characterize the mass and excitation energy of the compound nuclei formed in these incomplete fusion processes. This work was extended to higher bombarding energies for the $^{129}$Xe + Ti and Cu reactions at 26 and 31 MeV/nucleon [39]. An incomplete fusion model calculation which incorporated statistical emission from the hot products reproduced the following experimental data: the elemental cross sections, the emission velocities of the decay products, the center-of-mass angular distributions, and the source velocity distributions.

At low excitation energies complex fragment emission is quite rare. This implies that studies using complex fragments are ill suited to measure the yield of collisions that result in nuclei with low excitation energy. In the interpretation of $^{129}$Xe+Ti and Cu and $^{139}$La+Ti and Ni collisions, the authors claimed that the source velocity distribution was consistent with incomplete fusion processes; however, no events were observed with $v_{source}$ above 90% of the velocity of the beam. The low-mass-transfer events populating this region were not observed because the product nuclei primarily de-excite via light particle evaporation and result in evaporation residues.

Since heavy residues result from compound nuclei with low excitation energy, they should be a good tool to study the small mass transfer limit of the incomplete fusion process. (In this discussion, compound nucleus will mean any hot nucleus that has distributed the excitation energy among all the available degrees of freedom.) Measurement of residue production resulting from incomplete fusion allows for the quantitative testing of the incomplete fusion model over the entire range of mass transfers. The studies mentioned above, which used a heavy projectile nucleus and a light target

---

*Present address: UCSD, Department of Chemistry-0314, 9500 Gilman Drive, La Jolla, CA 92093.
†Present address: EG&G Energy Measurements, Washington Aerial Measurements Division, P.O. Box 380, Suitland, MD 20752.
‡Present address: LPC, Boulevard du Marechal Juin, 14050 Caen Cedex, France.
§Present address: Department of Physics and Astronomy, Mississippi State University, Mississippi State, MS 39762.
//Present address: Cyclotron Institute, Texas A&M University, College Station, TX 77845.
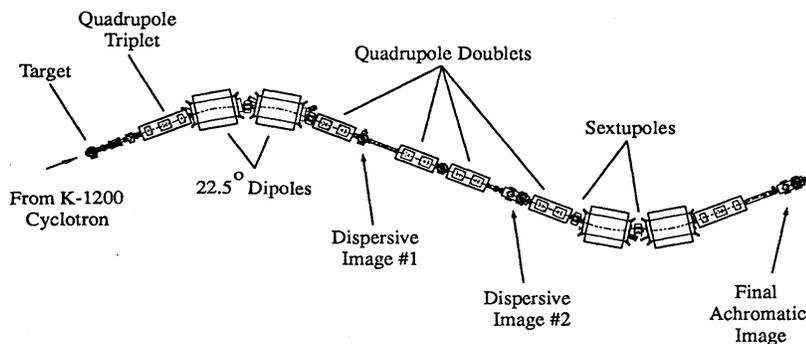
52     1462

FIG. 1. Schematic layout of the A1200 spectrometer.

nucleus, were unable to detect fragments with $Z$ values near that of the projectile since the detectors were placed at large center-of-mass angles to avoid elastically scattered beam particles. As a result, the model calculations that have been successful in predicting the complex fragment production have not been tested for high $Z$ values. Since these heavy residues contain the bulk of the yield for very asymmetric entrance channels, only a small portion of the total reaction cross section for these reactions has been measured. In addition, since the isotopic distribution of the complex fragments has not been previously measured, the isotope production predictions of the models have not been tested.

In the present work, the production cross section for heavy residues from the reactions of 26, 40, and 50 MeV/nucleon $^{129}$Xe + Be, C, and Al has been measured. To perform this measurement, a magnetic spectrometer was placed at $\sim$0 mrad in the laboratory frame and was used to measure the time of flight, the bend radius, the $\Delta E$, and the total energy of each fragment produced in the reaction. The heavy residues were identified in $Z$ and $A$. For each isotope, the absolute cross section and momentum distribution were determined.

This study provides a determination of the relative amounts of incomplete and complete fusion that is complementary to that obtained in the complex fragment studies. Events with very low excitation energy were easily measured since no fissionlike decay was required. The isotopic yields were compared with the predicted yields from two models. Combining the present data with previous data, experimental cross sections spanning almost the entire range of $Z$ values produced in these reactions have now been measured.

## II. EXPERIMENTAL METHOD

The K1200 cyclotron at Michigan State University accelerated beams of $^{129}$Xe ions to 26, 40, and 50 MeV/nucleon. The acceptance of the spectrometer ranged from 0 to 24 mrad in the laboratory frame and covered approximately 50% of the solid angle in this angular region. A schematic diagram of the A1200 spectrometer [41] is shown in Fig. 1. The A1200 spectrometer consists of 14 superconducting quadrupoles and four superconducting dipoles. Four sextupoles are used for higher-order optical corrections. The A1200 spectrometer has an angular acceptance of 0.8 msr, 3% momentum acceptance, and a maximum rigidity of 5.4 T m.

In this study, the reaction products were identified with a

technique similar to that used by Mohar et al. [42] and Bazin et al. [43]. This technique uses event-by-event measurements of the $\Delta E$, the $E_{total}$, the time of flight, and the magnetic rigidity to give unambiguous isotope identification.

The $^{129}$Xe beams bombarded targets of Be, C, and Al at the object point (labeled "target" in Fig. 1) of the A1200 spectrometer. The reaction products were collected and transported through the mass separator. At the first dispersive focus, labeled "image No. 1" in Fig. 1, a gas multistep detector [44] measured the position of each fragment. This detector also provided the start time for the time-of-flight measurement and is capable of better than 0.4 ns timing resolution and 1.6 mm position resolution, corresponding to 1 part in 2000 momentum resolution.

In order to measure the $Z$, $E_k$, $\theta$, and $\phi$ (nuclear charge, kinetic energy, and emission angles, respectively) of each ion, a set of detectors was placed at the final achromatic image of the mass separator. Two parallel plate avalanche counters (PPAC's) measured the position of each ion with 1 mm resolution and were separated by 420 mm. The measured positions were used to calculate $\theta$ and $\phi$. A 0.0001-cm-thick Bicron BC404 scintillating foil was mounted on a plastic light guide and optically coupled to a photomultiplier tube (PMT). The PMT signal from this detector was combined with the time information from the multistep detector at image No. 1 to measure the time of flight of the ions over the 13.811 m flight path. With this pair of detectors, a time-of-flight resolution of about 0.6 ns was obtained for the reaction products. A four-element silicon detector telescope provided $\Delta E$ and total energy measurements for each ion. Nuclear magnetic resonance probes in each of the dipole magnets were used to determine the magnetic fields.

### A. Calibration and isotope identification

The detection system was calibrated by transporting various primary beam analogs directly through the A1200 spectrometer. These beams have very similar charge-to-mass ratios and are commonly used to calibrate detector systems [45]. Since the reaction products were highly stripped when exiting the target, an Al target was used to strip the calibration beams. These ions with known energies and masses were used to calibrate the image No. 1 (horizontal) position measurement ($X$) versus the rigidity and the detector telescope. The flight time was calibrated by setting all the magnets so that the beam traveled along the central trajectory of
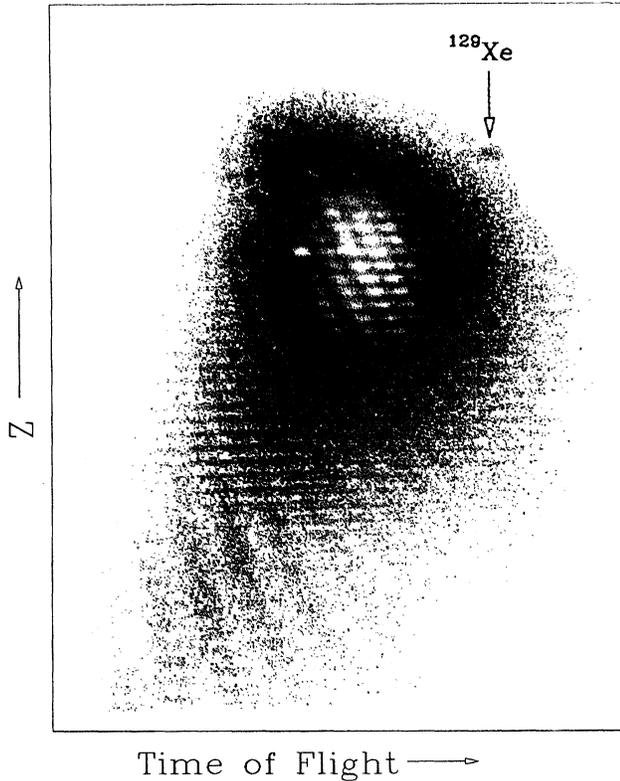
FIG. 2. Measured $Z$ versus time of flight for the 50 MeV/nucleon $^{129}$Xe + Al reaction.

the A1200 magnetic spectrometer, where the path length could be determined most accurately.

The calibration of the silicon detectors was performed in two stages. The initial energy loss calibration relied on ionizing trace impurities in the electron cyclotron resonance source that were extracted and accelerated in the K1200 cyclotron. Low beam intensities (100–1000 particles/s) were required since these calibration beams impinged directly on the detector telescope. Beams used were $^{65}$Cu$^{14+}$, $^{83}$Kr$^{18+}$, $^{97}$Mo$^{21+}$, $^{130}$Xe$^{29+}$, and $^{134}$Xe$^{29+}$ at 50 MeV/nucleon; $^{84}$Kr$^{17+}$ and $^{94}$Mo$^{19+}$ at 40 MeV/nucleon; and $^{86}$Kr$^{14+}$ and $^{92}$Mo$^{15+}$ at 26 MeV/nucleon. The energy lost in each detector by each calibration beam was calculated using standard energy-loss tables [46]. These calculated energy losses in each detector were plotted versus the measured peak position. This first stage energy-loss calibration proved adequate to provide an initial $Z$ calculation using the equation

$$Z = a(\Delta E \, E_{\text{total}})^{1/3} + b\Delta E. \qquad (1)$$

The $Z$ of each ion was calculated using the $\Delta E$ values from the first and second elements of the Si telescope. This procedure provided a redundant $Z$ determination for each ion, and the two calculations were averaged to improve the $Z$ resolution.

The first stage isotope identification and an improved energy-loss calibration were obtained by plotting the extracted $Z$ value versus the measured time of flight (see Fig. 2). This two-dimensional scatter plot shows the resolved elements as horizontal ridges. Since the A1200 spectrometer accepts a small momentum range (only $\pm 1.5\%$ of the central momentum), the individual isotopes of a given element are separated in time and appear as bumps along each ridge. There is one complication in this simple picture. An ion with a given mass-to-charge ratio $A/q$ is only slightly separated in time of flight from ions with the same $Z$ but having $(A+2)/(q+1)$ or $(A-2)/(q-1)$. This separation is about 0.4 ns, which is less than the experimental timing resolution of 0.6 ns. Therefore, it was not possible to separate isotopes with very similar $A/q$ by gating on this spectrum only. Elastically scattered beam particles were also present in this spectrum, indicating the position of the $^{129}$Xe ions. Furthermore, peaks in the time dimension for each $Z$ value were visible and well resolved. For the 40 and 50 MeV/nucleon runs at low rigidity, a vertical line of spots was produced at small time of flight due to a sequence of ions with $(A/q)=2$. With this characteristic reference line, the peaks for the lower $Z$ values ($20 \leqslant Z \leqslant 30$) were easily assigned to a given isotope, as these ions should be fully stripped at these high beam energies.

For the second stage of the calibration, 18 isotopes from various regions of this two-dimensional spectrum were chosen as calibration isotopes. Each selected ion was also required to travel along the central ray of the spectrometer by a software gate on the image No. 1 position. By requiring this condition, the energy of each ion could be easily calculated and the selected ion separated from other ions with similar $A/q$ values. This software condition restricted ions at the image No. 1 $X$ position to be within 3 mm of the central bend radius. Energy spectra from each silicon detector for each selected isotope were obtained. The error in $E_{\text{total}}$ calibration was typically less than 0.5%.

The second stage $Z$ calibration was obtained by using the improved energy-loss calibrations. The final experimental $Z$ resolution for the 40 MeV/nucleon data is shown in Fig. 3 [$\sigma(Z) = 0.36$ electron charge unit]. This calibration procedure was repeated for each beam energy and similar $E_k$, $Z$, $A$, and $Q$ resolutions were obtained in each case.

The mass of each ion was calculated from its measured total energy and time-of-flight data using the equation

$$A = \frac{E_{\text{total}}}{931.496(\gamma - 1)}, \qquad (2)$$

where $A$ is in atomic mass units and $E_{\text{total}}$ is in MeV. By substituting this equation into

$$B\rho = \frac{m\beta\gamma}{q}, \qquad (3)$$

where the usual relativistic parameters are

$$\beta = \frac{v}{c}, \qquad (4)$$

$$\gamma = \frac{1}{\sqrt{1-\beta^2}}, \qquad (5)$$

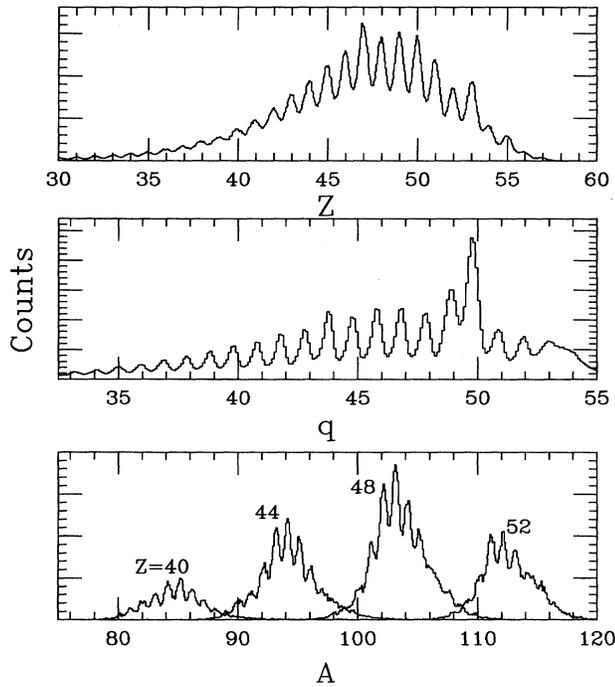where $v$ is the ion velocity and $c$ is the speed of light, and solving for $q$, one obtains

FIG. 3. The top frame shows the typical $Z$ resolution obtained in the 40 MeV/nucleon $^{129}$Xe + Al reaction, while the middle frame shows the typical $q$ resolution, and the bottom frame shows the typical $A$ resolution.

$$B\rho = 3.107\,11 \beta\gamma \frac{A}{q}, \quad (6)$$

$$q = \frac{3.107\,11}{931.496} \frac{E_{total}}{B\rho(\gamma-1)} \beta\gamma, \quad (7)$$

where $q$ is in units of electronic charge and $B\rho$ is in tesla meter. A histogram of the calculated $q$ is shown in Fig. 3 and indicates the good resolution achieved [$\sigma(q)=0.28$ electron charge units]. Since $q$ must be an integer and the mass resolution was limited by the error in the total kinetic energy measurement, the calculated $q$ was rounded to the nearest integer and the mass was recalculated using an integer $q$ in the equation

$$A = \frac{B\rho q}{3.107\,11 \beta\gamma}, \quad (8)$$

giving $A$ in atomic mass units again. A typical mass spectrum is shown in Fig. 3 and indicates the good mass resolution achieved [$\sigma(A) = 0.35$ amu].

### B. Momentum distribution calculation

The momentum $p$ of each particle was calculated using the equation

$$p = 931.496 \frac{B\rho q}{3.107\,11A}, \quad (9)$$

where the calculated $A$ and $q$ values are used. The momentum distributions of the reaction products are much wider than the 3% momentum acceptance of the A1200 spectrometer. To cover the entire momentum range, a number of runs were made using different magnetic field settings. Each run had central momenta differing by 2% from the neighboring runs. The momentum acceptance was not uniform at 100% across the full momentum range. It has been shown [47] that the momentum acceptance of the A1200 spectrometer drops by 10% at 1% from the central ray and as much as 30% at 1.5% from the central ray. To correct for the limited acceptance, the momentum distribution for each run was multiplied by the reciprocal of the acceptance function.

Four $p$-$i$-$n$ diodes were placed symmetrically around the target and were used to measure the beam current. The count rate of the $p$-$i$-$n$ diodes was related to the beam current so that the absolute beam flux for each run was known. The momentum distributions from each run were normalized using the beam flux and then added together. Some gaps in the distributions were caused by the tremendous amounts of scattered beam at a few particular momenta. The edges of the measured momenta were located and each gap was filled by interpolating between the edges. This final correction permitted the compilation of momentum distributions for all the ions with $Z > 39$.

The momentum distributions of interest are actually the distributions for each isotope as it exits the target rather than the distributions of each ion at the focal point. To produce this isotopic momentum distribution, all the momentum distributions for the charge states of each isotope must be summed. Since the ions have passed through the start detector, the charge state of the ion may have been changed at this point. Ion-optical calculations showed that, if the charge state of an ion changed in the start detector, the focus for that ion occurred at a different point at the final image of the spectrometer [48]. The focus of charge-changed ions was displaced horizontally from the original focal point of the spectrometer by about 4 cm for the case of $q=50$ and $\Delta q=1$. This displacement caused the charge-changed ions to miss the silicon detector stack and thus they were not observed. To account for this loss, it was assumed that ions passing through the start detector recreated their equilibrium charge state distribution. Charge state equilibrium was attained for 50 MeV/nucleon $^{129}$Xe in carbon for all thicknesses greater than 1 mg/cm$^2$. This assumption was checked by measuring the charge state distribution for 1.0, 1.3, and 2.0 mg/cm$^2$ thick carbon foils. The measured charge state distribution did not change as a function of carbon foil thickness. Since the start detector is made of plastic foils and filled with iso-octane, carbon is a good approximation of its material composition. The areal thickness of the start detector was 1 mg/cm$^2$, and thus the assumption of the start detector recreating charge state equilibrium is reasonable. To create the final isotopic momentum distribution, the distributions for each charge state of an isotope were summed after the correction for charge change in the start detector had been applied. Figure 4 shows the momentum distribution for each charge state of $^{104}$Sn after corrections and the final summed momentum distribution.

This process yields the momentum distribution for each isotope over the angular range of 0–24 mrad. Since the re-
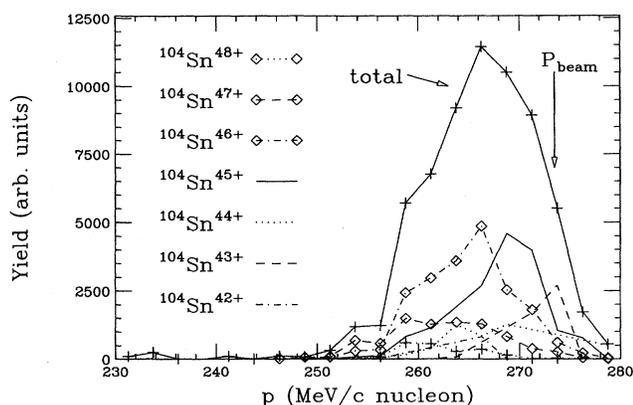
FIG. 4. Momentum distribution for $^{104}$Sn from the 40 MeV/ nucleon $^{129}$Xe + Al reaction shown as a solid line. The distributions for each charge state are shown in various textures.

action products were distributed over a wider angular range, to extract the absolute yield of an isotope the effects of the limited angular acceptance must be removed. The angular spread of the ions was calculated assuming an incomplete fusion reaction mechanism. (See Sec. IV B for a description of the incomplete fusion calculation.) The width of the angular distribution results primarily from evaporation from the fused product. This width was only slightly changed by using a Boltzmann-Nordheim-Vlasov model of the reaction mechanism. (See Sec. IV B 3 for a description of the Boltzmann-Nordheim-Vlasov calculation.) Figure 5 shows the A1200 angular acceptance in the top frame. The calculated laboratory angular distributions for various $Z$ values are shown in the bottom frame. The fraction of the angular distribution that was contained within the angular acceptance of the A1200 spectrometer was calculated. The yields for each isotope were then multiplied by the reciprocal of the acceptance fraction. This final correction allowed the compilation of the absolute production cross section for each isotope from each reaction. The error in the absolute yield of each isotope from the counting statistics is typically less than 10%. However, the beam current measurement did not work very well and a factor of 4 systematic error in the absolute beam flux is possible. This results from a poor normalization of the $p$-$i$-$n$ diode count rate to the beam current.

### III. EXPERIMENTAL RESULTS

#### A. Momentum distributions

The momentum of each particle was calculated using the equation

$$p = 931.496 \frac{B\rho q}{3.107\,11A} = 931.496\beta\gamma c, \qquad (10)$$

where $p$ is the momentum in MeV/$c$ nucleon. The $\beta\gamma$ product was not calculated from the time-of-flight measurement but rather deduced from the $B\rho$ calculated from the NMR reading and the bend radius measured at image No. 1. This $B\rho$ determination was used because it was more accurate than the time-of-flight measurement. Typical momentum dis-
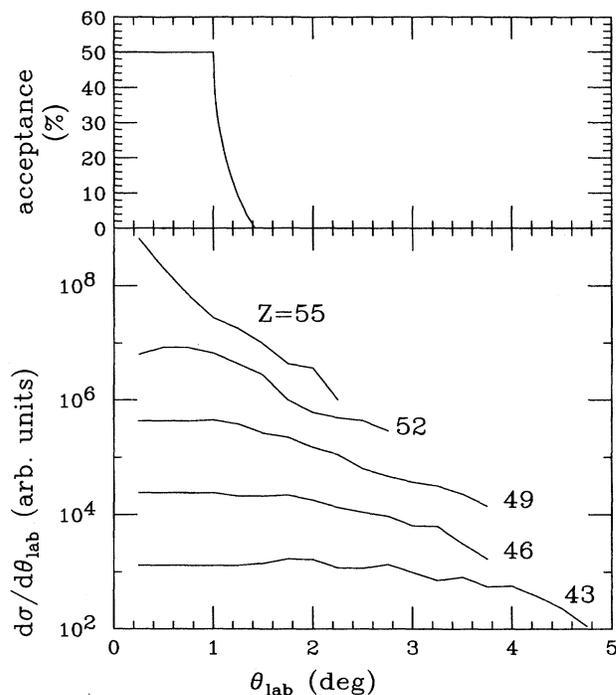


FIG. 5. The angular acceptance of the A1200 spectrometer is shown in the top frame. Calculated angular distributions from the incomplete fusion model for selected elements are shown in the bottom frame.

tributions from the 50 MeV/nucleon $^{129}$Xe + Al reactions are shown in Fig. 6 for representative light, medium, and heavy isotopes of selected elements. The momentum distributions for each isotope of Sn and Mo are shown in Fig. 7. The fluctuations in the curves are due to low statistics. For a given element, the momentum distributions of the light mass isotopes peak near the momentum per nucleon of the beam, whereas the momentum distributions of the heavier isotopes peak at lower values. The momentum distributions of the heaviest isotope of the elements close to $Z=40$ extend almost down to the momentum per nucleon corresponding to complete fusion. These differences are most distinct in the data from the $^{129}$Xe+Al reaction and are less apparent in the data from the Be and C targets due to the smaller range of momentum between the momentum per nucleon of the beam and that of the center of mass. The data from the two lower beam energies exhibit similar behavior. (Momentum distributions for all elements for the 50, 40, and 26 MeV/nucleon $^{129}$Xe + Be, C, Al reactions are contained in [49].)

#### B. Isotopic distributions

The absolute cross section for the production of each isotope was determined by integrating its momentum distribution. The measured isotopic cross sections for each of the nine target-beam energy combinations are shown in Figs. 8, 9, 10, and 11 for isotopes with $Z > 39$. The overall dependence of the isotopic cross sections on bombarding energy and target mass is best seen in Fig. 11. The yield for the
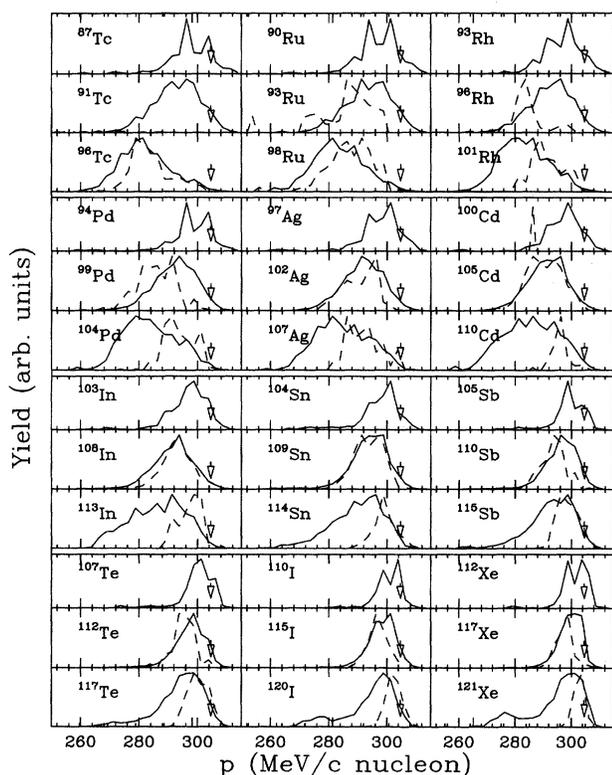
FIG. 6. The solid curves are momentum distributions for representative light, medium, and heavy isotopes of all elements from the 50 MeV/nucleon $^{129}$Xe+Al reaction. The dashed curves are the results of an incomplete fusion model calculation. The arrow is at the momentum of the beam in each frame. The momentum of the center of mass for this system is 251.9 MeV/$c$ nucleon.



FIG. 7. Momentum distributions for all isotopes of Sn and Mo for the 50 MeV/nucleon $^{129}$Xe+Al reaction.

lighter elements produced in the reaction of the 26 MeV/nucleon $^{129}$Xe with the light targets is quite low (as also indicated in Fig. 10), and the cross sections are more uncertain. The low counting statistics lead to the large fluctuations in the data between neighboring isotopes (e.g., a factor of 5 for $Z$=40 in the 26 MeV/nucleon $^{129}$Xe + Be reaction).

A peak at $A$=129 is clearly visible in the $Z$=54 curve in Figs. 8, 9, 10, and 11. This peak arises from (elastic) scattering of the incident beam. The yield of fragments with low $Z$ values increases as the target mass increases at a given beam energy (see Fig. 11). The yield of these light fragments also increases as the beam energy increases. Both of these trends parallel an increase in center-of-mass energy, as shown in Table I. Generally, events with high excitation energies emit a larger number of particles while deexciting than do events with low excitation energies and this leads to increased yields of lower $Z$ value elements.

To better see the dependence of the isotopic yields on bombarding energy the isotopic cross sections in the $A$ versus $Z$ plane are shown in Fig. 12. The stable isotopes are marked with solid squares in these figures. The stair-stepping line indicates the proton-rich limit of the known nuclei. These figures clearly show that the isotopes produced in these reactions all have lower $A/Z$ ratios than the stable nuclei, indicating substantial neutron evaporation. Also visible
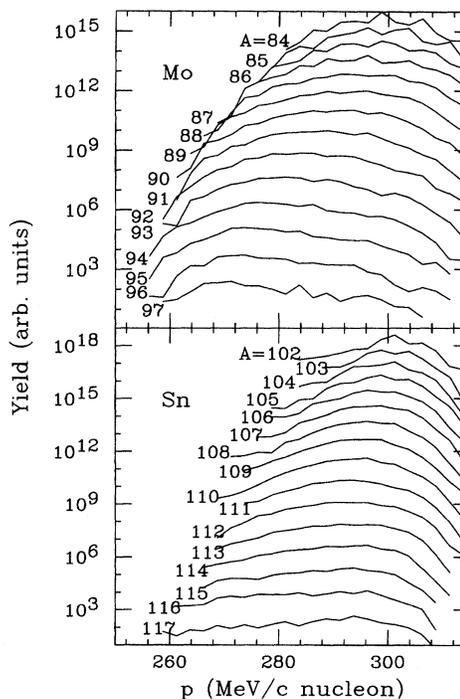
in these figures is the increasing yield of low $Z$ value fragments with increasing center-of-mass energy.

In Fig. 13, the average mass of each element is shown for the 50 MeV/nucleon $^{129}$Xe + Be, C, and Al reactions. In the lower portion of this figure, the width of the mass distribution for each element is shown. This figure shows that the average mass and the width of the mass distribution for each element are independent of the target. A similar target independence is also seen for the other two beam energies.

Previous $\gamma$-ray spectroscopy studies of heavy residues have extracted the average $Z$ value for each isobar. The line following the average $Z$ value for each isobar is comparable to the ridge in the isotopic cross section distribution from the current data set. Similar energy $^{12}$C + $^{107-109}$Ag reactions have been studied using $\gamma$-ray spectroscopy [28]. This allows a comparison between the $^{12}$C + Ag data and the present $^{129}$Xe + C data. In Fig. 14, the average $Z$ value for each isobar from the reaction of $^{12}$C + Ag [28] (diamonds) is compared with the isotopic cross section distributions from the $^{129}$Xe + C (contours) reactions measured with the A1200 spectrometer. Although the ranges of elements measured only partially overlap, it is clear that the isotopes produced in the $^{129}$Xe-induced reactions are significantly more proton rich than those produced in the $^{12}$C + Ag reaction. The $^{12}$C + Ag reaction products become less proton rich with increasing bombarding energy, whereas the yields from the $^{129}$Xe + C data show no such dependence on the bombarding energy. These differences may be the result of the inability of the $\gamma$-ray spectroscopy to measure very short-lived nuclei; however, it is difficult to prove that this is the cause of the differences.
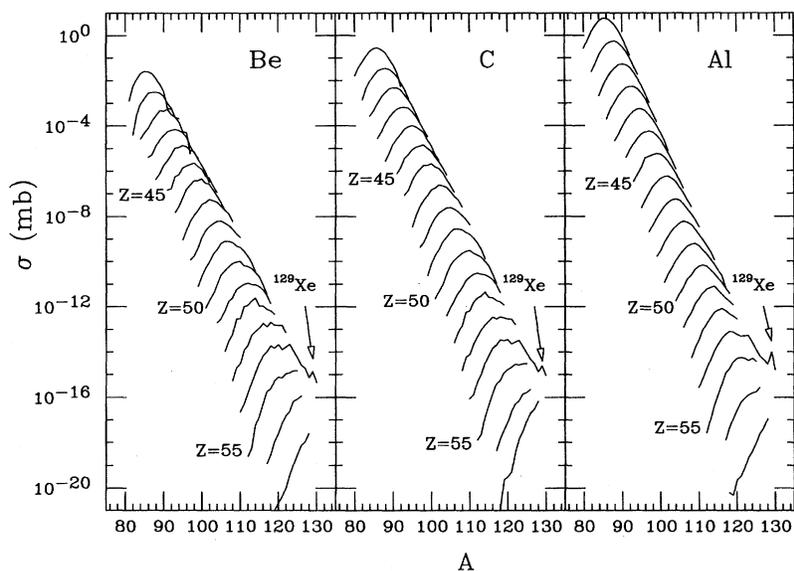
FIG. 8. Isotopic cross sections for the 50 MeV/nucleon reactions. The curves join the cross sections for all the isotopes of a given element. All curves, except that for $Z=40$, are offset from their neighbors by an order of magnitude so that they do not overlap.

A previous study measured part of the isotopic yields from the 70 MeV/nucleon $^{92}$Mo + $^{58}$Ni reaction [50]. These yields are shown as histograms in Fig. 15. Since this system was studied using a magnetic spectrometer, it is not subject to the experimental restrictions of the $\gamma$-ray spectroscopy. However, these data were collected over a narrow range of magnetic rigidities and may be biased towards those nuclei with $A = 2Z$. For comparison, the isotopic cross sections for the same elements from the 50 MeV/nucleon $^{129}$Xe+Al reaction are shown as continuous curves. The centroid values of these distributions are close, but the isotopes produced in

the $^{92}$Mo + $^{58}$Ni reaction are slightly more proton rich, as might be expected given the more proton-rich target and projectile combination.

### C. Elemental and isobaric yields

Previous studies of similar systems have measured the elemental and isobaric cross sections. In this study, the isotopic cross sections can be obtained by integrating the isotope's momentum distribution. The isotopic cross sections for all of the isotopes of each element can be summed to
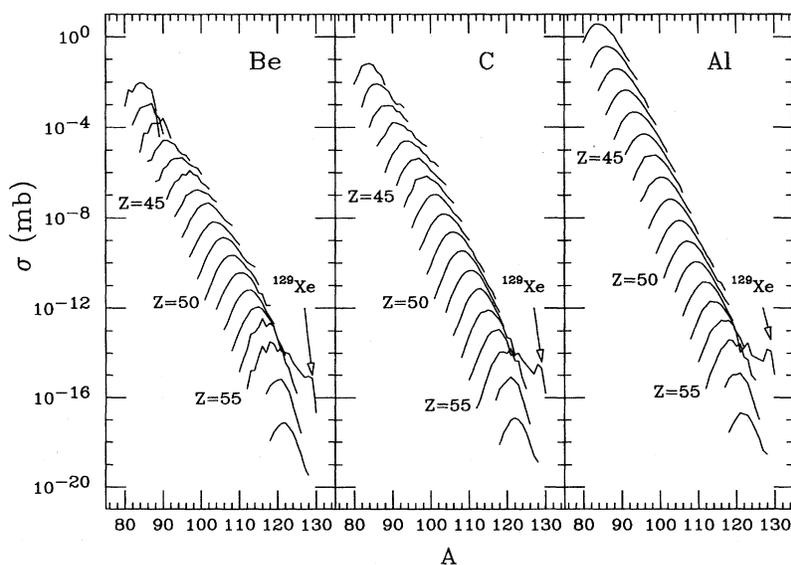


FIG. 9. Isotopic cross sections for the 40 MeV/nucleon reactions. The curves join the cross sections for all the isotopes of a given element. All curves, except that for $Z=40$, are offset from their neighbors by an order of magnitude so that they do not overlap.
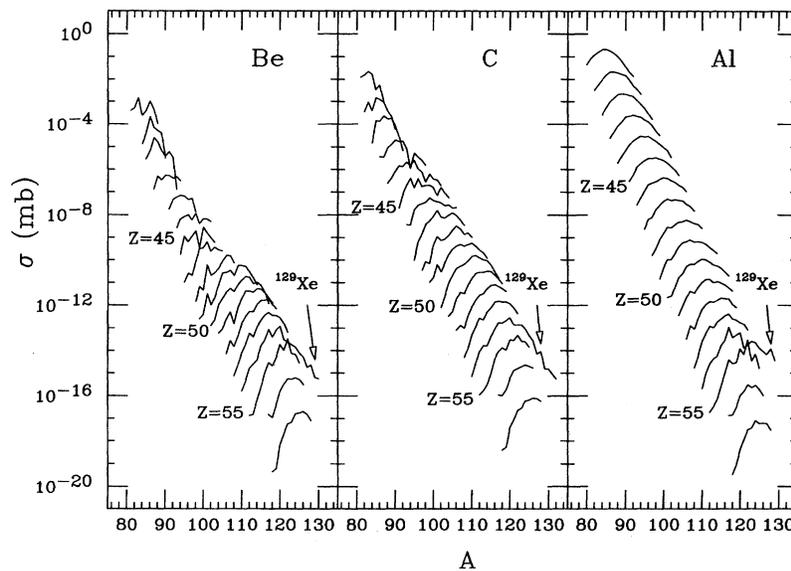
FIG. 10. Isotopic cross sections for the 26 MeV/nucleon reactions. The curves join the cross sections for all the isotopes of a given element. All curves, except that for $Z=40$, are offset from their neighbors by an order of magnitude so that they do not overlap.

produce the elemental cross sections. These elemental cross sections are shown by the diamonds in Fig. 16. The elemental cross section distributions become wider at higher beam energies and for heavier target nuclei. Previous measurements of the elemental cross sections from similar systems are plotted as pluses [36,38,39,40]. Note that the cross sections measured in the present work cover a range of elements not measured in the complex fragment studies. Although the elements that have been previously measured do not significantly overlap the current data, the two data sets seem to be consistent. Notice that a large fraction of the total reaction cross section was missed in the previous studies of complex fragments.

The isobaric cross sections are the most accurately determined yields from $\gamma$-ray spectroscopy studies because the calculation of these yields requires the smallest number of assumptions. The isotopic cross sections for all the isotopes of each isobar from the present study were summed to produce isobaric cross sections. These isobaric cross sections are shown by the continuous curves in Fig. 17. Also shown in Fig. 17 are the isobaric cross sections (measured using $\gamma$-ray spectroscopy) from similar reactions measured by Lleres [51]. These data sets are shown as pluses and times symbols with the $^{129}$Xe-induced reaction from the present work that most closely approximates the $^{124}$Sn reaction. Since the reactions presented for comparison have similar target and projectile masses and bombarding energies and the center-of-mass energy is large in all cases, the nuclear structure effects for a particular beam and target combination should be minimized and the resulting isobaric cross sections should be and generally are similar. The $^{129}$Xe + Al data compare better with the $^{20}$Ne + $^{124}$Sn results than with the $^{40}$Ar + $^{124}$Sn results. This is reasonable because the excitation energy of the compound nucleus rapidly increases with the mass symmetry of the entrance channel. There remains a deficit in the isobaric yields from the $\gamma$-ray spectroscopy

studies. Such a deficit may be due to the difficulty of measuring nuclei near stability with the $\gamma$-ray technique or may result from the systematic error in the beam current in the present work.

Figures 16 and 17 show that the shapes of the cross section distributions for the present and previous studies are similar. This agreement is consistent within the experimental uncertainties associated with the different measurements. The data from the present study at 26 MeV/nucleon appears to be low in comparison to the previous work. This may be due to the complications of measuring the many atomic charge states present at the lowest beam energy. The overall agreement also gives confidence in proceeding to compare the absolute cross sections with the results of model calculations.

### D. Z versus velocity distributions

Previous studies of complex fragment emission have presented distributions of $Z_{total}$ versus $v_{source}$ [21,29,39,36]. The source velocity $v_{source}$ is defined as

$$v_{source} = \frac{\sum m_i v_i}{\sum m_i}, \tag{11}$$

where $m_i$ and $v_i$ are the mass and velocity, respectively, of the $i$th detected complex fragment. These distributions were used to determine the velocity of the source of the complex fragments. Similar information about the source of the heavy residues in the present work can be extracted by integrating the isotopic momentum distributions over $A$ and converting momentum to velocity to produce comparable $Z$ value versus velocity distributions. These distributions for all the reaction systems in the present work are shown in Fig. 18. For comparison, complimentary complex fragment data are also shown. (The $^{139}$La data have been shifted down by three
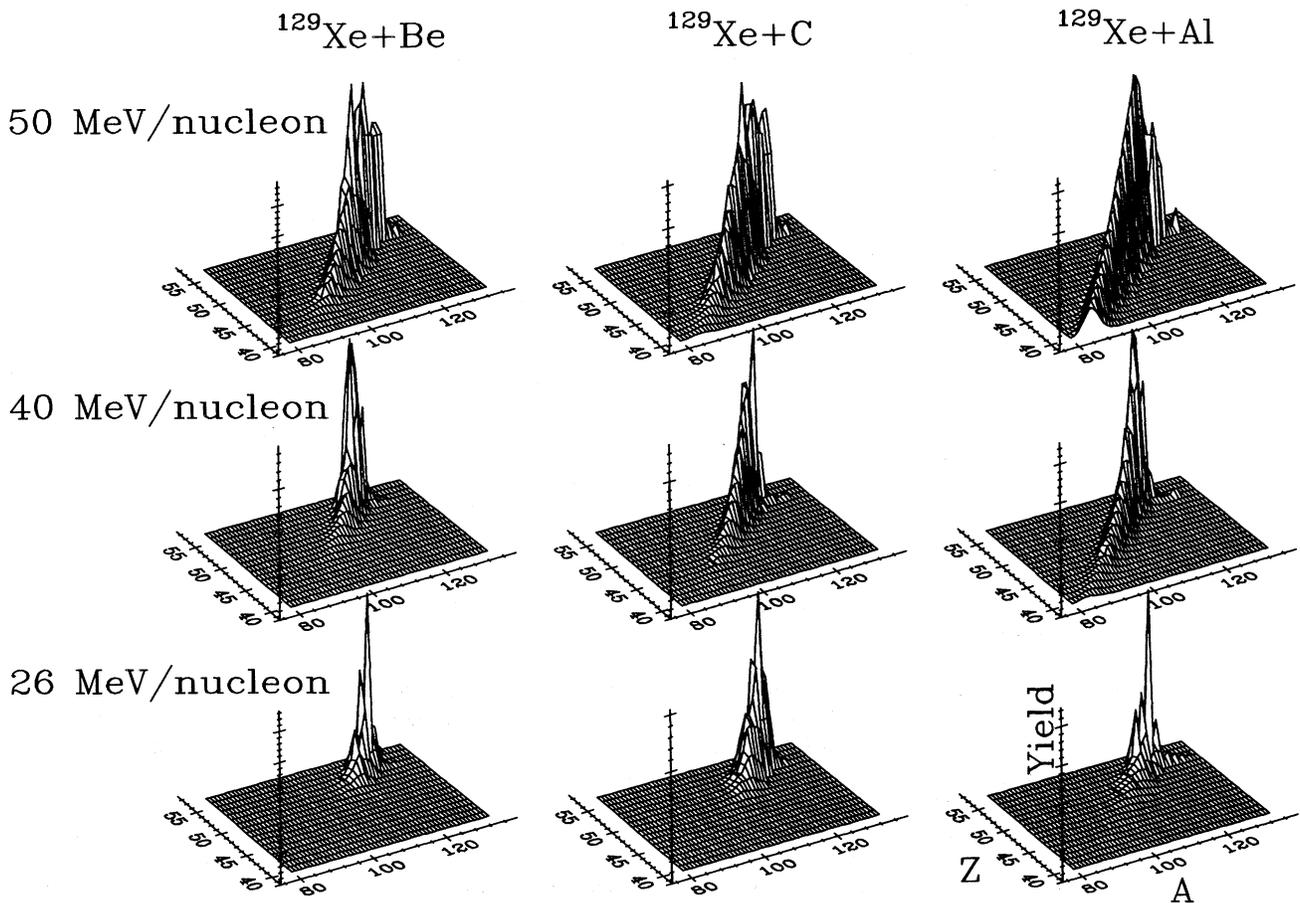
FIG. 11. The three-dimensional surfaces of the isotopic cross sections are shown. Note the variation of the shape of the surface with target and bombarding energy. The axis going to the right represents $A$, that going to the left represents $Z$, and the vertical axis represents the yield.

units of $Z$ to account for the difference in $Z$ values between $^{139}_{57}$La and $^{129}_{54}$Xe.) The data at higher velocity in each frame of Fig. 18 are from this work; the data at lower velocities, noted as "CF," are taken from the referenced complex fragment studies. Figure 18 clearly shows the complimentary nature of the present measurements to the studies of the complex fragments. The cross section contours mesh together well and indicate that a complete measurement of the reaction requires both techniques.

### E. Summary of the experimental results

The data for the $^{129}$Xe-induced reactions were presented and compared to similar data from previous measurements of

TABLE I. Maximum excitation energy possible for each beam energy and target combination (in MeV).

| Beam energy and target (MeV/nucleon) | Be | C | Al |
|---|---|---|---|
| 26 | 220 | 285 | 580 |
| 40 | 335 | 440 | 890 |
| 50 | 420 | 550 | 1115 |

similar reaction systems. In general, the new data are consistent within experimental errors. The new information available in the present data includes the elemental cross sections for the high $Z$ value elements ($Z \geqslant 39$), the yield of fragments at velocities near that of the beam, the isotopic cross sections for part of the elemental yield range ($Z \geqslant 39$), and the momentum distributions for the high $Z$ value isotopes. By combining the present data with the previous data, elemental cross sections from $Z=6$ to $Z=57$ are available. The present experiment measured fragments with a range of velocities not seen in the complex fragment data.

## IV. DISCUSSION OF DATA AND MODELS

Previous studies of the 14–50 MeV/nucleon $^{129}$Xe + C and $^{139}$La + C reactions have demonstrated that one source of complex fragments is the statistical decay of a compound nucleus [17,38,39]. At low bombarding energies ($E/A < 25$ MeV), the compound nucleus is formed in complete fusion reactions. At higher bombarding energies ($E/A > 30$ MeV), incomplete fusion of the reaction partners forms a range of compound nuclei with different masses and excitation ener-
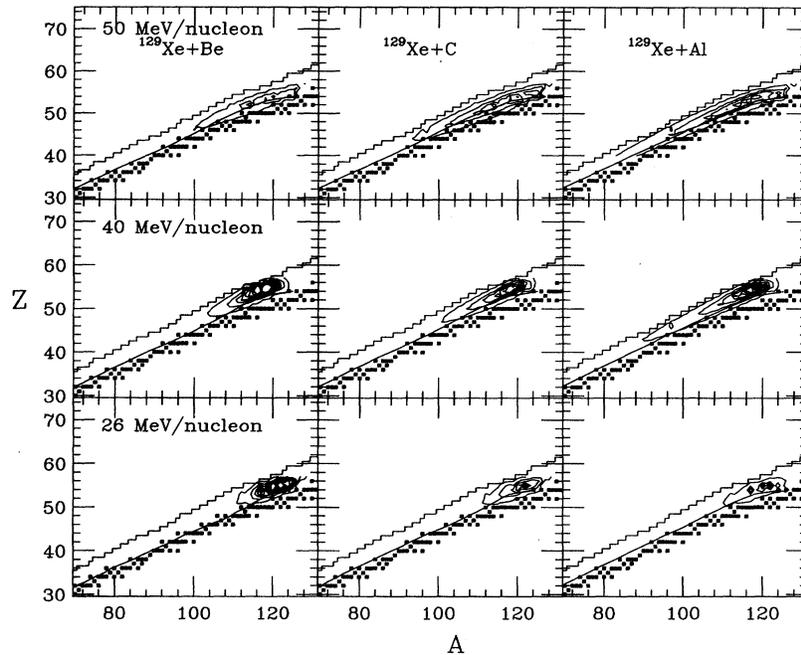
Start

FIG. 12. Contour plots of the isotopic cross sections in the $A$ versus $Z$ plane. Solid squares indicate the positions of the stable isotopes. The stair-stepping line shows the proton-rich limit of the known isotopes. The solid curve just to the proton-rich side of the stable isotopes is the result from an incomplete fusion calculation.

gies. The complex fragments from these reactions have isotropic center-of-mass angular distributions $(d\sigma/d\theta)$ and center-of-mass emission velocities dominated by the Coulomb repulsion of the two decay partners. These two features indicate a relaxed and long-lived source (source lifetime $\gg$rotational period). In addition, the source velocities ($v_{source}$) extracted from analysis of both single-particle inclu-



FIG. 13. The average $A$ and the full width at half maximum (FWHM) of the $A$ distribution for each element from the 50 MeV/nucleon $^{129}$Xe + Be (solid line), C (dashed line), and Al (dotted line) reactions. Note the independence of the average and width of the $A$ distribution on the target. The stair-stepping line shows the proton-rich limit of the known isotopes. Solid squares represent the positions of the stable isotopes.

sive data and coincidence data are consistent and fall within the range expected from the complete or incomplete fusion reaction mechanism. The $v_{source}$ value is used to calculate the amount of transferred mass and the excitation energy, which in turn is used in a statistical deexcitation model to calculate the complex fragment production cross sections. The agreement between the experimental and predicted cross sections, angular distributions, and emission velocities shows the validity of the compound nucleus source assumption.

As the present experiment is able to detect all the heavy residues produced in these reactions, several new questions can be addressed.

(1) From the experimental standpoint, do the heavy residues come from the same source as the complex fragments, or do they result from a different source?

(2) From the theoretical standpoint, if the heavy residues have the same source as the complex fragments, can the models that successfully predicted the complex fragment production also predict the heavy residue production?

(3) From the practical standpoint, what is the source of the extremely proton-rich nuclei observed recently? The proton-rich nuclei are $^{61}$Ga, $^{62,63}$Ge, $^{65}$As, $^{66}$Se, $^{69}$Br, and $^{75}$Sr from 65 MeV/nucleon $^{78}$Kr + $^{58}$Ni [42,52]; $^{78}$Y, $^{82}$Nb, $^{84,85}$Mo, $^{86}$Tc, and $^{89,90}$Ru from 70 MeV/nucleon $^{92}$Mo + $^{58}$Ni [50]; $^{94,95}$Ag from 70 MeV/nucleon $^{106}$Cd + $^{58}$Ni [53]; and $^{101,102}$Sn from 58 MeV/nucleon $^{112}$Sn + Ni [54]. These nuclei are important to nuclear structure studies, and understanding their production mechanism would facilitate these studies.

To address these questions, the data are first qualitatively examined for signatures of the reaction mechanism (Sec. IV A). Then, two models of the reaction mechanism are
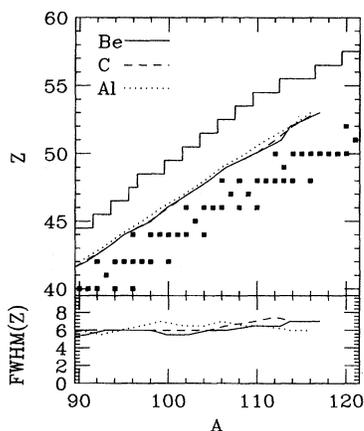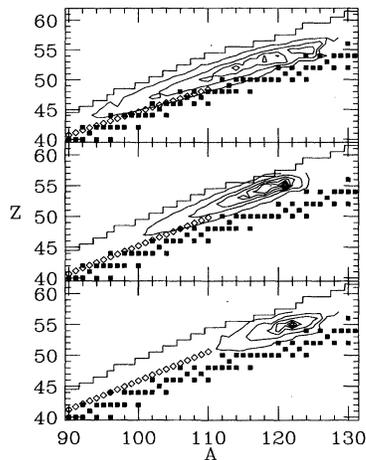
FIG. 14. Contour plots of the isotopic cross sections in the $A$ versus $Z$ plane. In all three panels, the solid squares represent the positions of the stable isotopes, the stair-stepping line shows the proton-rich limit of the known isotopes, and the diamonds on the proton-rich side of the stable isotopes are the average atomic number for each isobar from the reaction of C + Ag measured by Chung, Chu, and Porile [28]. The top frame compares the results from the reactions of 50 MeV/nucleon $^{129}$Xe + C and 45 MeV/nucleon $^{12}$C + Ag, the middle frame contains the results of 40 MeV/nucleon $^{129}$Xe + C and 35 MeV/nucleon $^{12}$C + Ag, and the bottom frame shows the results from 26 MeV/nucleon $^{129}$Xe + C and 25 MeV/nucleon $^{12}$C + Ag.

compared to the previous and present data sets to test how well these models quantitatively describe the data (Sec. IV B). It will be shown that the isotopic cross sections and momentum distributions from the present study do, in fact, provide a new, previously unavailable test of reaction model predictions.

## A. The velocity as a function of Z

In previous complex fragment studies, two-dimensional distributions of the cross section as a function of $Z_{total}$ and $\mathbf{v}_{source}$ have been created, where $Z_{total}$ and $\mathbf{v}_{source}$ are the total charge and the center-of-mass velocity of the detected complex fragments, respectively. There are typically one to five heavy fragments and many light particles in the exit channel of the studied reactions. The heavy fragments move relative to one another with a well-defined velocity determined mainly by the Coulomb repulsion energy between the fragments. The evaporation of light particles either preceding or following the heavy fragment emission acts to increase the width of the $\mathbf{v}_{source}$ distribution. The kinematic skeleton of the source breakup is not altered by isotropic $(d\sigma/d\Omega)$ evaporation. Thus, the experimentally accessible $\mathbf{v}_{source}$ value corresponds closely to the velocity of the emitting source. For complete fusion reactions, $\mathbf{v}_{source}$ is equal to the velocity of the center of mass $(\mathbf{v}_{c.m.})$. In incomplete fusion reactions, only a fraction of the lighter nucleus fuses with the heavier nucleus. When the projectile is larger than the target, $\mathbf{v}_{source}$ is larger than $\mathbf{v}_{c.m.}$ but smaller than the velocity of the beam $(\mathbf{v}_{beam})$. The $\mathbf{v}_{source}$ is near the $\mathbf{v}_{beam}$ for small mass transfers, and the $\mathbf{v}_{source}$ is near the $\mathbf{v}_{c.m.}$ for nearly complete mass



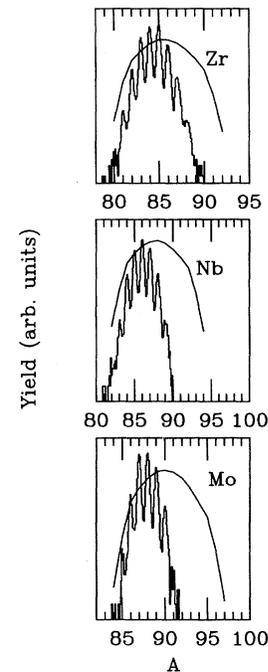FIG. 15. The mass yields from the 50 MeV/nucleon Xe+Al reaction are shown by the solid curves. The mass yields from the 70 MeV/nucleon $^{92}$Mo+$^{58}$Ni reaction are indicated by histograms.

transfers. Therefore, an accurate determination of $\mathbf{v}_{source}$ should allow one to infer the amount of mass transferred.

For the 18 MeV/nucleon $^{139}$La+C and the 26 and 31 MeV/nucleon $^{129}$Xe + C reactions [17,21,39], a single peak is observed in the reconstructed $\mathbf{v}_{source}$ distribution. Its centroid is at $\mathbf{v}_{c.m.}$. The isotropic center-of-mass angular distributions $(d\sigma/d\theta)$, the Coulomb-repulsion-dominated emission velocities, and the elemental cross sections of the complex fragments are all consistent with these reactions being dominated by complete fusion processes that result in compound nuclei. For the Xe(La) + Al and higher energy Xe(La) + C reactions (18 MeV/nucleon $^{139}$La + Al, 26 and 31 MeV/nucleon $^{129}$Xe + Al, and 35 to 55 MeV/nucleon $^{139}$La+ C, Al reactions [17,36,38,39,55]), again a single peak in the $\mathbf{v}_{source}$ distribution was observed, but the centroid value was between the values of $\mathbf{v}_{c.m.}$ and $\mathbf{v}_{beam}$, consistent with an incomplete fusion reaction mechanism. For the Xe(La) + Ti, Ni, and Cu reactions (18 MeV/nucleon $^{139}$La + Ti and Ni reactions and 26 and 31 MeV/nucleon $^{129}$Xe + Ti and Cu [21,39]), a range of values for $\mathbf{v}_{source}$ was observed, suggesting a broad range of mass transfers resulting from incomplete fusion reactions.

In the studies mentioned above, complex fragments emitted from compound nuclei have been detected. However, these compound nuclei can also deexcite by emitting only light particles $(Z \leq 2)$, leaving a single cold heavy residue. For low excitation energies, complex fragment emission is an unlikely deexcitation process; thus, experiments that measure only the complex fragment production cross sections have missed a large portion of the primary yield. The $Z_{total}$ versus $\mathbf{v}_{source}$ distribution for complex fragment coincidence
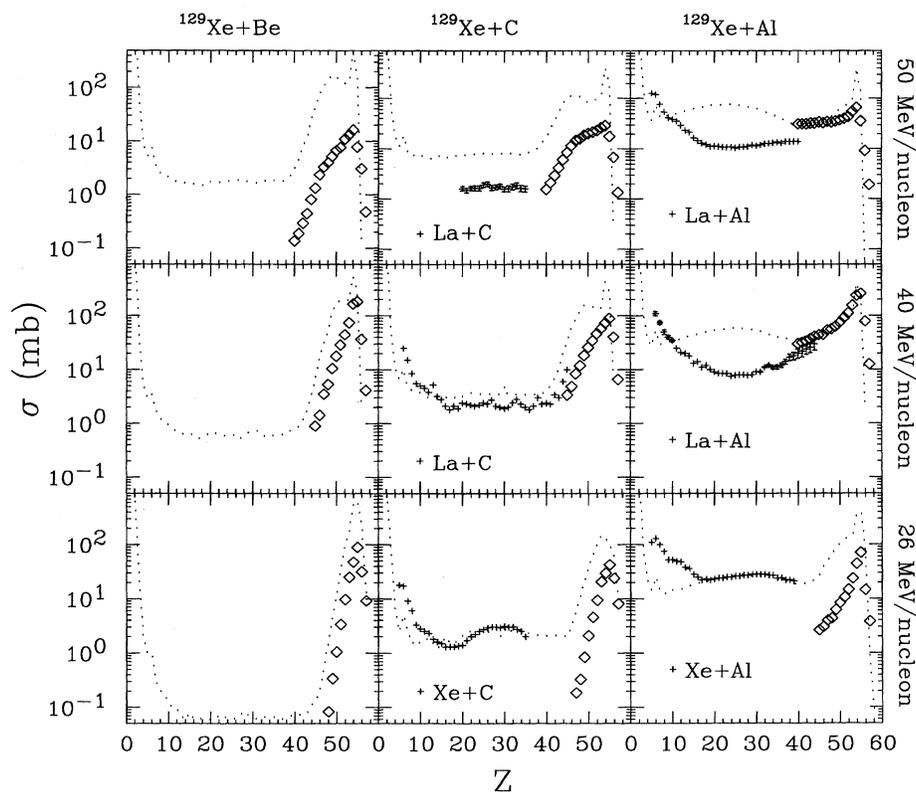
FIG. 16. The measured elemental cross sections are shown as diamonds. Complex fragment cross sections from similar reactions are shown as pluses. Shown as a dotted line are the elemental cross sections from an incomplete fusion model calculation.

events should have the same correlations as the $Z$ value versus velocity distributions for the heavy residues, since both evaporation residues and complex fragments can result from the same nuclear reaction mechanism. The experimentally determined $Z$ value versus velocity distributions for the heavy residues are shown in Fig. 18. The distributions of $Z_{total}$ versus the $v_{source}$ derived from the complex fragment coincidence events from similar reactions are also shown in Fig. 18.

The shapes of the $Z$ value versus velocity distributions qualitatively support the incomplete fusion reaction mechanism, as illustrated in Fig. 19. The solid line represents the range of values of velocity and $Z$ value for the primary products that result from the incomplete fusion reactions of a large projectile nucleus with a small target nucleus. The excitation energy of these products increases systematically with decreasing velocity. The amount of excitation energy depends directly on the amount of mass transferred and on the bombarding energy. Tables II and III show the excitation energies for $^6Li$ and $^{12}C$ transfers at 26, 40, and 50 MeV/nucleon in the $^{129}Xe$ + Al reaction. The excitation energies are calculated using the incomplete fusion model described in Sec. IV B 1. This excitation energy is lost primarily through evaporation. Statistical decay calculations show that, on average, a charge is evaporated for approximately every 50 MeV of excitation energy. Using this result, the average evaporation residue $Z$ value can be calculated. The result of this calculation is also shown in Tables II and III. Notice that

the same mass transfer at a higher bombarding energy results in higher excitation energy and a lower average residue $Z$ value. In Fig. 19, the dotted line qualitatively indicates the nuclear charge of the incomplete fusion residues after evaporation for a low bombarding energy. As the bombarding energy increases, the excitation energy produced in the reaction increases and the locus of the final fragments rotates clockwise because of increased charged-particle evaporation. The two dashed lines schematically indicate the nuclear charge after evaporation for two higher bombarding energies.

The heavy residue data from the 26 MeV/nucleon reactions have almost no variation in the centroid value of the $Z$ distribution as a function of velocity (see Fig. 18). This indicates that there is a balance between the charge gained in the incomplete fusion process and the charge lost via evaporation during the deexcitation. In the higher energy reactions, the centroid value of the $Z$ distribution decreases as the velocity decreases, indicating that more charge is lost by evaporation than is gained in the incomplete fusion process.

The incomplete fusion reaction mechanism also qualitatively explains the range of velocities seen for each data set in Fig. 18. Within a given bombarding energy, small mass transfers result in primary fragments with high velocities, small amounts of excitation energy, and low angular momenta. The low excitation energy and angular momentum give the resulting compound nucleus a low complex fragment emission probability, and thus a large probability of producing an evaporation residue. In contrast, large mass
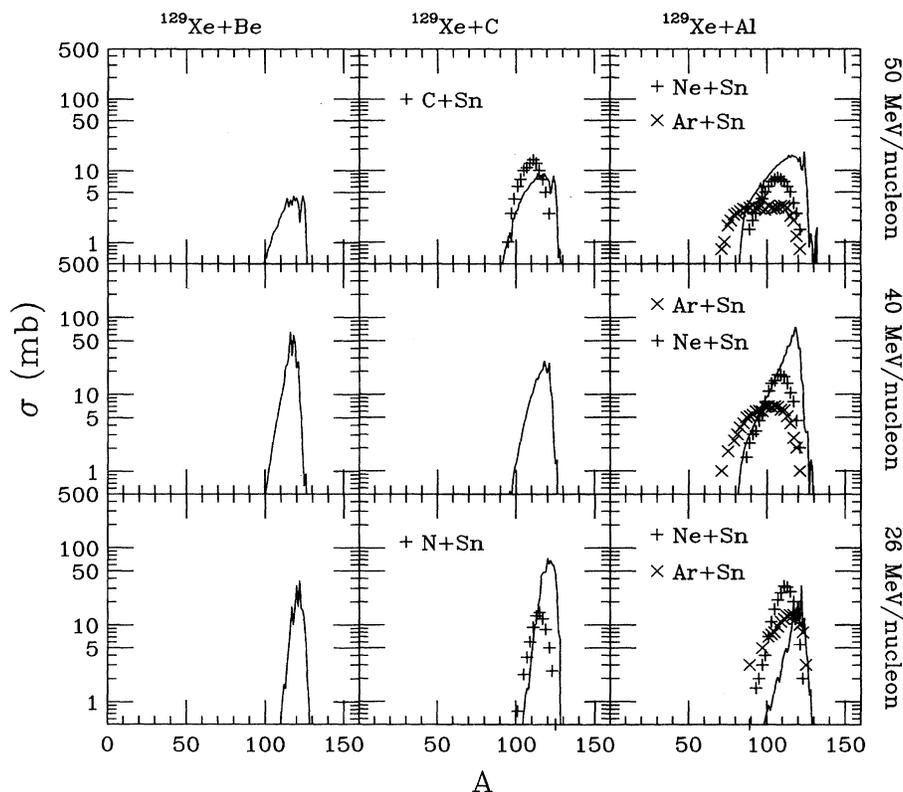
FIG. 17. The isobaric cross sections for each of the target-beam energy combinations from this work are shown by the curves. Also shown as pluses and times symbols are the cross sections from 30 MeV/nucleon $^{14}$N + $^{124}$Sn, 49 MeV/nucleon $^{12}$C + $^{124}$Sn, 30 MeV/nucleon $^{20}$Ne + $^{124}$Sn, 40 MeV/nucleon $^{20}$Ne + $^{124}$Sn, 49 MeV/nucleon $^{20}$Ne + $^{124}$Sn, 27 MeV/nucleon $^{40}$Ar + $^{124}$Sn, 35 MeV/nucleon $^{40}$Ar + $^{124}$Sn, and 44 MeV/nucleon $^{40}$Ar + $^{124}$Sn as indicated in each panel.

transfers result in primary fragments with lower velocities, higher excitation energies, and higher angular momenta. The higher excitation energy and angular momentum give a higher complex fragment emission probability and a lower probability of producing an evaporation residue.

In the present experiment, when the incomplete fusion product emits a complex fragment, the resulting decay products are rarely detected, as the recoiling nuclei are usually outside the spectrometer acceptance. Thus, the depletion of heavy residues at low velocities (i.e., near $v_{c.m.}$) in the $^{129}$Xe + Al reactions results from high excitation energies in the primary fragments. The primary fragments' concomitant high probability of emitting a complex fragment results in their low probability of detection in the current experiment. In contrast, the high probability of emitting a complex fragment gives large mass transfer, low velocity events a higher detection probability in complex fragment experiments. This is why the complex fragment data in Fig. 18 are near $v_{c.m.}$ for each reaction. Thus, the present $Z$ value versus velocity distributions for the heavy residues fit nicely with the $Z_{total}$ versus $v_{source}$ distributions for the complex fragments (i.e., detecting the heavy residues is a good way to measure the cross section of small mass transfer events and detecting the complex fragments is a good way to measure the cross section of large mass transfer events). The combination of these data sets gives a complete picture of the reaction mechanism

that can be understood within the framework of the incomplete fusion reaction mechanism. The qualitative agreement between the model and the data suggests that this reaction mechanism deserves further detailed investigation.

### B. Model calculations

In this section, the predictions from two models are discussed and compared with the data. These models are the incomplete fusion (ICF) model and the Boltzmann-Nordheim-Vlasov (BNV) model. It has been shown that an incomplete fusion reaction mechanism qualitatively explains the data (see Sec. IV A) and both the ICF and BNV models can produce incomplete fusionlike reactions. The BNV model is able to simulate preequilibrium emission of nucleons, whereas the ICF model cannot. Preequilibrium emission can have significant effects at the bombarding energies used in the present work and thus the BNV model is a useful companion to the ICF model. Neither of these models is capable of calculating the deexcitation of the excited fragments. To remedy this problem, both models are coupled to a statistical decay model which simulates the deexcitation process.

Both models have been used previously to predict the data from similar reactions. The ICF model [38] has been successful in explaining many features of complex fragment emission from the 26 MeV/nucleon $^{129}$Xe + C, Al, Ti, and
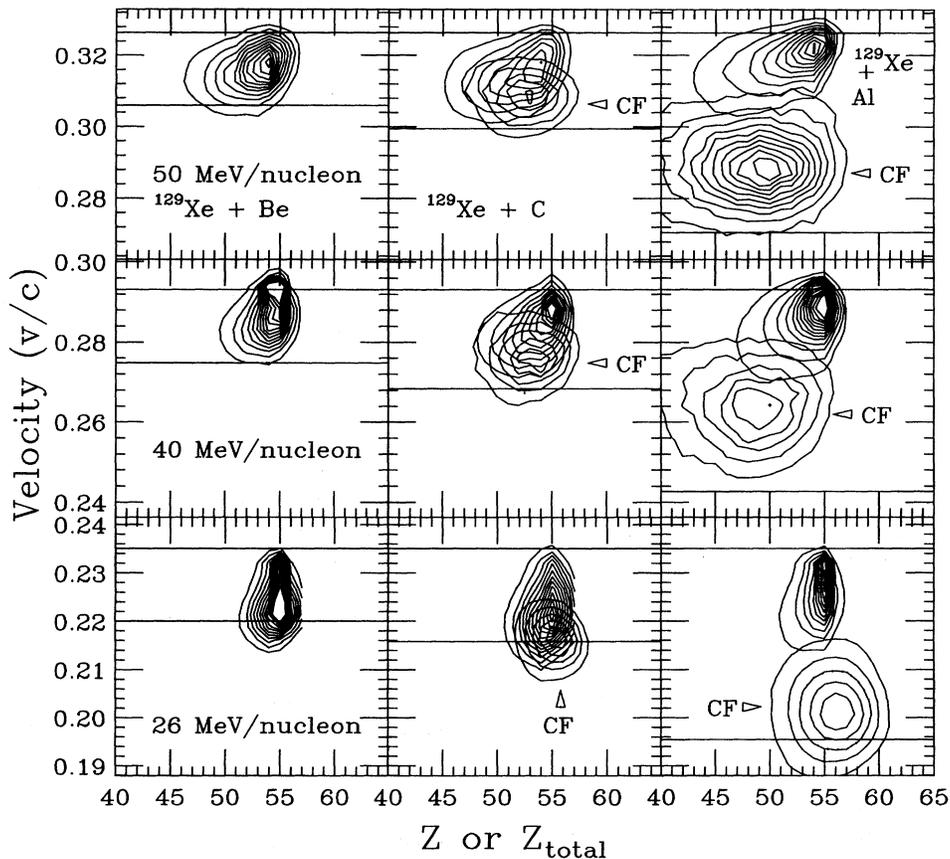
FIG. 18. Cross section contours in the $Z$-velocity plane for all systems measured in this work. Also shown are complex fragment ("CF") data from 26 MeV/nucleon $^{129}$Xe+C and Al, 40 MeV/nucleon $^{139}$La+C and Al, and 50 MeV/nucleon $^{129}$Xe+C and Al. The upper horizontal line in each frame lies along the velocity of the beam. The lower horizontal line in each frame lies along the velocity of the center of mass for that system.

Cu reactions [39]. The BNV model has been successful in explaining certain aspects of the complex fragment data from the 55 MeV/nucleon $^{139}$La + Al [56,57] and 50 MeV/ nucleon $^{129}$Xe + C, Al, V, Cu, Y, and Au reactions [58].

### 1. Incomplete fusion calculation

Predicting the final residue products from the incomplete fusion reaction involves two stages. The first stage is the incomplete fusion process. The second stage is the statistical decay of the excited fragments produced in the incomplete fusion process. (For clarity during the following discussion, "ICF model" refers only to the model of the first stage, whereas "ICF calculation" refers to the result of using the primary fragments from the ICF model as input to the statistical decay calculation.)

In the first stage of the calculation, a geometrical incomplete fusion model [38] is used to describe the dynamics of the reaction in which two sharp spheres represent the colliding nuclei. The energetics of fragment formation is assumed to be dominated by the increase in the surface area of the fragments. Since the surface area created by breaking the smaller nucleus into parts is less than the area created by breaking the larger nucleus into parts, it takes less energy to

break the smaller nucleus. To account for this, the model forces the overlapping nuclear matter to be sheared from the smaller target nucleus and fuses it onto the the larger projectile nucleus to produce a compound nucleus plus a cold spectator. The model generates values for the $Z$, $A$, excitation energy, final spin $J$, and the laboratory velocity of each of the reaction partners. The excitation energy is calculated from the energetics of the surface creation and from the mass transfer. $J$ is calculated from the relative motion of the centers of mass of the projectile and the lump of mass transferred from the target.

In the second stage of the calculation, the large excited primary fragment formed in the incomplete fusion process is assumed to deexcite statistically. The statistical decay of each fragment is simulated by using the Monte Carlo computer code GEMINI [17], in which all possible binary decays of the compound nucleus, from light particle emission to symmetric division, are considered. After each binary division, further decay of the resulting excited fragments is followed until all the available excitation energy is exhausted. Following the emission of a heavy fragment, the remaining excitation energy is divided under the assumption of equal temperatures in the two fragments. To calculate the spin of
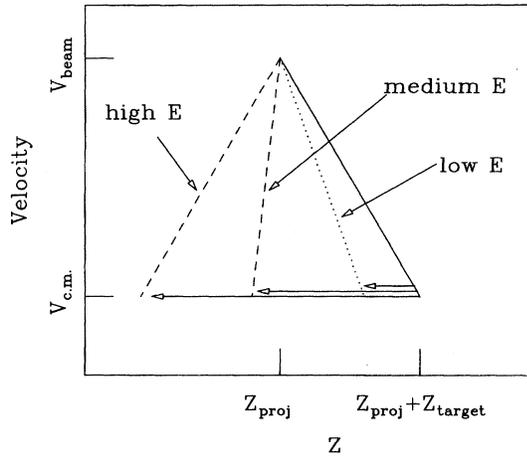
FIG. 19. Schematic representation of the effect of light charged-particle evaporation on the correlation between the velocity and the $Z$ of the incomplete fusion product. $Z_{proj}$ is the $Z$ value of the projectile. The solid line represents the locus of the velocities of the primary products from an incomplete fusion process. The short horizontal arrow to the dotted line shows the effect of evaporation on these products for low bombarding energies. The dashed lines show the loci of the velocities of the products after evaporation for higher bombarding energies.

each fragment, the angular momentum is partitioned in the sticking limit. Thermal fluctuations in both the division of the excitation energy and the partition of angular momentum are incorporated. The decay widths for the evaporation of light particles ($Z \leq 2$) are calculated using the Hauser-Feshbach formalism [59]. The decay widths for the emission of heavy fragments ($Z \geq 3$) are calculated in GEMINI by using the transition state formalism of Moretto [60]. Details of these calculations are described in [17].

An ICF calculation was carried out for each reaction studied in the present work. All the parameters of the statistical decay model were set to standard values. The only adjustable parameter in the ICF model was the radius parameter ($r_0$), used to calculate the size of the sharp spheres.

$$R_{\text{sharp sphere}} = r_0 A^{1/3}. \tag{12}$$

In this model, sharp-surfaced spheres were used to represent the nuclei. In reality, the nuclear surface is diffuse, and so $r_0$ was assumed to be slightly adjustable.

It has been shown that the ICF calculations are sensitive to the value chosen for the radius parameter [39]. Hanold *et al.* used $r_0$ as a fitting parameter in this ICF calculation to

TABLE II. Excitation energy and average residue $Z$ value for the transfer of a $^6$Li to form $^{135}$La in the $^{129}$Xe + Al reaction.

| Beam energy ($E/A$) (MeV) | Excitation energy (MeV) | Average residue $Z$ value |
|---|---|---|
| 26 | 175 | 53.5 |
| 40 | 250 | 52.0 |
| 50 | 310 | 50.8 |

TABLE III. Excitation energy and average residue $Z$ value for the transfer of a $^{12}$C to form $^{141}$Nd in the $^{129}$Xe + Al reaction.

| Beam energy ($E/A$) (MeV) | Excitation energy (MeV) | Average residue $Z$ value |
|---|---|---|
| 26 | 320 | 53.6 |
| 40 | 470 | 50.6 |
| 50 | 580 | 48.2 |

reproduce the complex fragment data from the 26 MeV/nucleon $^{129}$Xe + C, Al, Ti, and Cu reactions. The best agreement with the cross sections and the $Z_{total}$ versus $v_{source}$ distributions was obtained with a value of $r_0 = 1.10$ fm. In the present study, changing the radius parameter had no effect on the predicted average mass for each element. (The predicted average mass for each element is determined by the statistical decay calculation. See Sec. IV B 2.) The predicted elemental cross sections, however, were sensitive to $r_0$, as the cross section for production of the heavy residues increased 20% and the cross section in the $10 \leq Z \leq 30$ region increased 50% when $r_0$ was increased from 1.10 fm to 1.25 fm. The increased cross section results from the increased range of impact parameters that led to collisions and a greater fraction of these collisions led to primary products with high excitation energy when $r_0$ was 1.25 fm. The high excitation energy gives a higher complex fragment emission probability and thus leads to the larger increase in the complex fragment cross sections. A radius parameter of 1.10 fm was found to give the best agreement with the data from the previous study, and it also gave good agreement with the present data set.

The results from the ICF calculations can be compared to the cross section data in Figs. 16, 20, and 12 and the momentum distributions in Fig. 6. (Figure 16 shows the elemental cross sections from the ICF calculation as dotted curves.) Possible systematic experimental errors make the absolute cross sections uncertain by up to a factor of 4. (The error in the magnitude of the yields primarily results from a poor measurement of the integrated beam current.) The magnitude of the cross sections from the ICF calculation is somewhat variable, since $r_0$ was taken to be adjustable. Therefore, the shape of the predicted elemental cross sections is a more sensitive test of the calculation than the magnitude. For the heavy residues, the cross section distributions predicted by the ICF calculation generally have the same shape as the experimental cross section distributions, but the predicted cross sections are larger in magnitude. The ICF predictions for the $^{129}$Xe + C data agree with the complex fragment data at 26 and 40 MeV/nucleon but overpredict the complex fragment yields at 50 MeV/nucleon. The ICF calculation for the $^{129}$Xe + Al reaction only agrees with the complex fragment cross sections at 26 MeV/nucleon. The calculation for the 40 and 50 MeV/nucleon $^{129}$Xe + Al reactions predicts complex fragment yields within an order of magnitude of the data, but the shape of the distribution is incorrect. Overall, the ICF calculation reproduces all the cross sections except for the complex fragment cross sections from the 40 and 50 MeV/nucleon $^{139}$La + Al reactions.

The measured distributions of cross sections for fragments with $Z > 39$ as a function of $Z$ value and velocity are
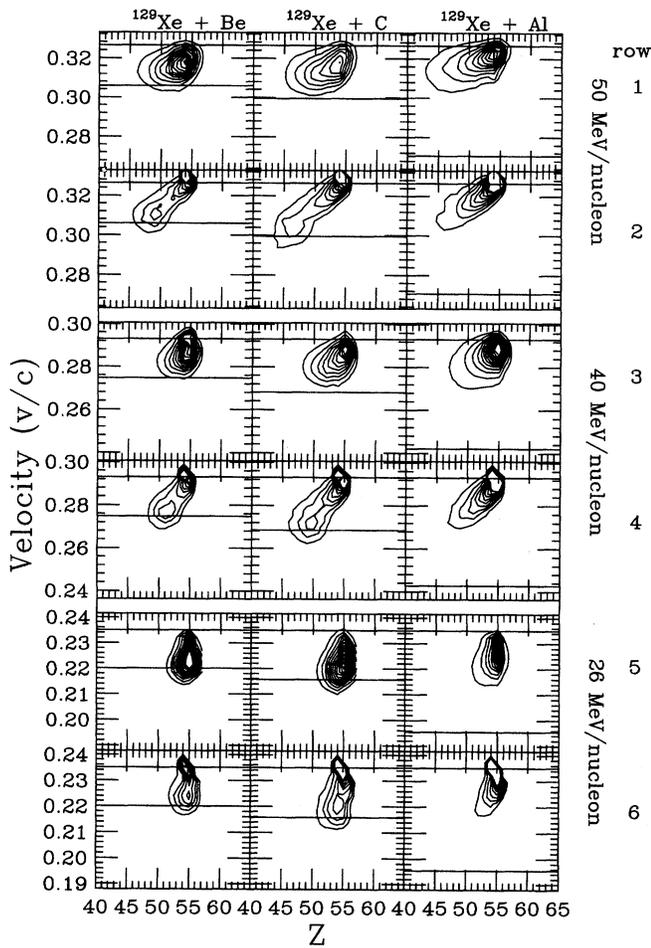
FIG. 20. The distribution of cross section as a function of $Z$ value and velocity are shown in the first, third, and fifth rows. The second, fourth, and sixth rows show the prediction of the incomplete fusion calculation. The upper horizontal line in each frame corresponds to the velocity of the beam. The lower horizontal line in each frame corresponds to the velocity of the center of mass for that reaction.

shown in the first, third, and fifth rows in Fig. 20. The second, fourth, and sixth rows show the predictions of the incomplete fusion calculation. Notice that the overall shape of the velocity distribution is predicted by the calculation. The clockwise rotation of the data with increasing bombarding energy is also expected from the ICF model. The ICF calculation also predicts the centroid value of the $Z$ distribution correctly for all the targets and beam energies in this study. The width of the $Z$ distribution for the 26 MeV/nucleon reactions is well reproduced, but the predicted width is too small by almost a factor of 2 for the 40 and 50 MeV/nucleon reactions.

The cross sections as a function of $Z$ value and velocity are consistent with the incomplete fusion reaction mechanism, but the isotopically resolved momentum distributions provide a more detailed test of the model predictions. The momentum distribution for each isotope was extracted from the data, and the results are shown in Figs. 6 and 7. The
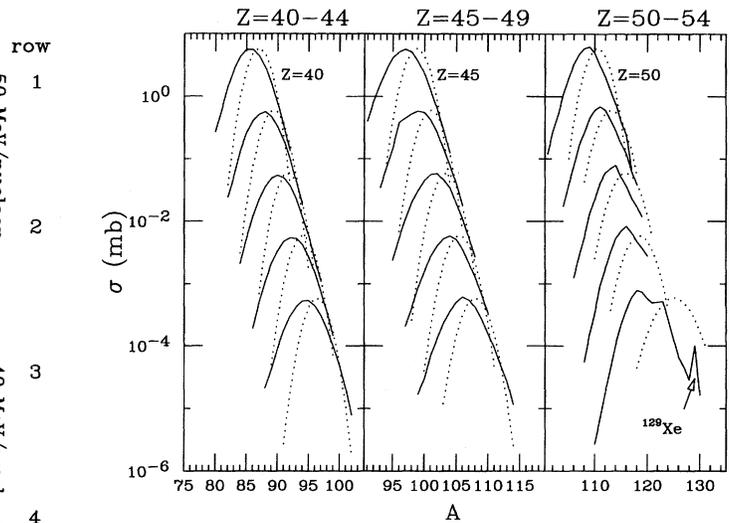


FIG. 21. Experimental isotopic cross sections for the 50 MeV/ nucleon $^{129}$Xe + Al reaction are shown as solid curves. The predictions of the incomplete fusion calculation are shown as the dotted curves for the same reaction. The cross section for each element has been offset by an order of magnitude from its neighbors. The magnitude of the calculation has been scaled in this figure for easier comparison of the centroid values and the widths of the distributions with the data.

shape of the momentum distribution changes slowly with the mass of a given element (see Fig. 7); therefore, only the momentum distributions for a representative light, average, and heavy isotope of each element are presented in Fig. 6. The experimental momentum distributions can be compared to the predictions from the ICF calculations. The calculated momentum distributions are shown as dashed curves on Fig. 6. Note that the model predicts the very proton-rich isotopes to have less than 50 nanobarn production cross section in these reactions. This is why there are no predictions shown with the momentum distributions for the proton-rich isotopes. The shape and width of the calculation's distributions are close to the shape and width of the experimental distributions, but the predicted centroid values of the momentum distributions for the heavy isotopes are too large.

Figure 21 shows the isotopic cross section distributions from the ICF calculation and from the experimental data. (Figure 16 shows that the predicted elemental cross sections from the ICF calculation are too large. This implies that the total of the predicted isotopic cross sections for each element is also too high. The magnitude of the predicted isotopic cross sections shown in Fig. 21 is scaled to match the maximum heights of the experimental cross section distributions. This was done to allow easy comparison of the centroid values and widths of the predicted and experimental distributions.) The predicted average isotope of a given element has, typically, two more neutrons than the experimentally determined average isotope of that element. (Alternatively, Fig. 21 could be made to join all the isotopes of each isobar rather than all the isotopes of each element. It would then appear that the calculation's average atomic number for each isobar is one atomic number less than the experimental av-

erage atomic number for each isobar.) Furthermore, the predicted width of the mass distribution of each element is smaller than the corresponding experimental width. Figure 12 shows as contours the isotopic cross sections for each reaction studied here. The predicted average mass for each element is shown as a solid line on these figures. The ridge in each isotopic cross section distribution is comparable to the solid line. The overprediction of the average mass of each element by 2 amu is seen for each system. Possible solutions of this disagreement are discussed in Sec. IV B 2.

Overall, the ICF calculation gives a qualitatively acceptable prediction of the results from this experiment. The shapes of the predicted elemental cross section distributions are correct for the heavy residues, and the predicted magnitudes of the cross sections are larger but are within the experimental uncertainty. The shapes of the cross section distributions as a function of $Z$ value and velocity are closely predicted by the calculation. The shapes of the calculated elemental cross sections for the complex fragments are correct for all the $^{129}Xe(^{139}La)$ + C reactions and for the 26 MeV/nucleon $^{129}Xe+Al$ reaction. The observed independence of the average mass for each element from the entrance channel (see Fig. 13) is predicted by the ICF calculation. The average mass of each element, the width of the mass distribution of each element, and the width of the $Z$ distribution as a function of velocity are not well reproduced, however. The causes of these differences are examined further in the next section.

### 2. GEMINI and the isotope predictions

The overprediction of the experimental average mass of each element and the underprediction of the widths of the final fragment distributions are the significant failings of the ICF calculation. Since changing the radius parameter ($r_0$) of the ICF model had no effect on these predictions, the statistical decay calculation was examined to determine whether it was the cause of these differences.

The $A/Z$ ratio of the final fragments resulting from statistical decay is decoupled from the $A/Z$ ratio of the primary fragment for sufficiently high excitation energies. Charity *et al.* [17] claimed that this decoupling occurs if the excitation energy is above 1 MeV/nucleon. In the present study, this excitation energy is easily reached for even small mass transfers. For the ICF model at 26 MeV/nucleon, this means transferring merely four nucleons, whereas at 50 MeV/ nucleon, only two nucleons need be transferred.

To demonstrate the decoupling of the initial and final $A/Z$ ratios at high excitation energies, the average mass of each element was calculated for two different systems. One system was very proton rich ($Z=67$, $A=149$, $E^*=580$ MeV, and $J_{max}=110\hbar$), and the other system was very neutron rich ($Z=67$, $A=166$, $E^*=580$ MeV, and $J_{max}=110\hbar$). The calculation used a $2J+1$ weighting at each $J$ and $J$ ranged from $J=0\hbar$ to $J_{max}$. For each element, the average residue masses from these two systems differ by less than one mass unit over most of the $Z$ range. This is shown in Fig. 22. A second, simpler statistical decay model that allowed only the emission of $\gamma$ rays and evaporation of neutrons, protons, and alpha particles was run to check the GEMINI predictions. The results from this code (LOTO [61]) are consistent with the GEMINI results. Thus, the step in the ICF + GEMINI calcula-
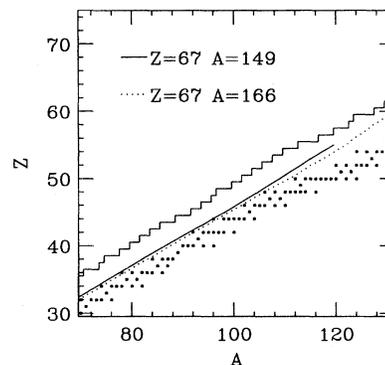


FIG. 22. The average masses of each element predicted by GEMINI for two different initial nuclei are shown. One system is very proton rich, $Z=67$ and $A=149$, and is shown as a solid line. The other system is very neutron rich, $Z=67$ and $A=166$, and is shown as a dotted line. Shown as the stair-stepping line is the proton-rich limit of the known isotopes. Solid squares mark the positions of the stable isotopes.

tion that determines the average mass for each element is the statistical decay calculation, since the $A/Z$ ratio of the final fragments from GEMINI is decoupled from the $A/Z$ ratio of the initial fragments input into GEMINI.

The isotopes predicted by GEMINI are less proton rich than the isotopes observed in the present work. Increasing the excitation energy of the initial fragments does not make the predicted final fragments more proton rich. Instead, increasing the excitation energy causes more evaporation, and the average residue mass decreases. This may indicate that the value of the binding energy for the neutrons used in the calculations is too high relative to the emission barrier for protons in proton-rich nuclei. The neutron and proton binding energies are unknown for these nuclei, since the masses of many proton-rich nuclei seen in this work have not been measured. An extended liquid drop model [62] of the ground state nuclear mass is used by GEMINI to calculate the neutron and proton binding energies for proton-rich nuclei. This mass model has a root-mean-squared error of 0.863 MeV for the ground state mass of the known nuclei. Small changes in the barriers for particle emission from the proton-rich nuclei may improve the agreement between the calculation and the data. For example, reducing the neutron binding energy of the proton-rich nuclei by 0.3 MeV reduces the average mass of each element by 1 amu. This change in the masses of the proton-rich nuclei is within the mass model's uncertainty, and thus the predicted average mass for each element can be brought into agreement with the experimental value.

In addition, there are other input parameters in the statistical decay calculation whose values are not well known. For example, the level density parameter ($a$) and the asymmetry parameter of the mass model are not well known. Small adjustments of these parameters may improve the agreement between the calculation and the data.

To investigate the effect of the level density parameter on the widths of the final fragment distributions, $a$ was varied in the GEMINI calculations from $a=A/7$ to $a=A/10$. For $a=A/7$, the predicted average mass for each element decreased slightly ($\langle A_{a=A/8.5}\rangle - \langle A_{a=A/7}\rangle=0.5$) and the width

of the isotopic cross section distribution decreased ($\sigma_{a=A/7}/\sigma_{a=A/8.5}=0.75$) relative to the predictions using $a=A/8.5$. With $a=A/10$, the predicted average mass for each element increased slightly $\langle A_{a=A/8.5}\rangle - \langle A_{a=A/10}\rangle = -0.5$ and the width increased ($\sigma_{a=A/10}/\sigma_{a=A/8.5} = 1.2$) relative to the predictions with $a=A/8.5$. When $a$ decreased, the width of the distribution increased, but not enough to reproduce the data. Furthermore, the disagreement between the experimental and predicted average masses of each element became larger. These two opposite effects do not allow the simultaneous reproduction of both the average isotope for a given element and the width of the mass distribution for that element by solely varying $a$.

Adjusting the binding energy for the neutrons changes the proton richness of the final fragments. Decreasing $a$ and decreasing the neutron binding energy have opposing effects on the proton richness of the final fragments. The neutron binding energy and $a$ were used together as fitting parameters to make the ICF predictions and the experimental values for the centroids and the widths of the final fragment distributions consistent. Agreement between the model predictions and the experimental data was achieved by reducing the neutron barrier by 2 MeV and setting $a$ equal to $A/15$. This large $a$ variation of these parameters does not seem physically justifiable.

The mass asymmetry parameter can change the neutron and proton binding energies so that they do not vary as strongly with the $A/Z$ ratio of the decaying nucleus. The final fragment distribution can be made broader by changing this parameter. Unfortunately, this change also destroys the mass model's ability to reproduce the known nuclear masses. This implies that varying the mass asymmetry parameter is not a good solution to the disagreement between the model predictions and the experimental data.

There are a few other options for improving the agreement between the calculations and the data. The $A/Z$ ratio of a nucleus with low excitation energy ($E^* \leqslant 30$ MeV) is not changed very much by the deexcitation process. If the model of the collision stage produced a distribution of primary fragments that was similar to the experimental distribution, and these fragments had low excitation energies, then the subsequent deexcitation by GEMINI would not alter the primary distribution. The agreement between the prediction and the data would be improved. Excitation energies this low, however, are produced for only the extremely peripheral collisions in the ICF model, and these collisions do not yield proton-rich primary fragments. This option is not available within the ICF model.

It was thought that the smaller predicted widths of the mass distribution for each element may result from the lack of fluctuations in the $A/Z$ ratio of the transferred mass in the ICF model. Therefore, fluctuations in the $A/Z$ ratio of the transferred mass were added to the ICF model. They had no effect on the final fragment distributions, however, since the final fragment $A/Z$ ratio from GEMINI is decoupled from the initial fragment $A/Z$ ratio.

It was thus found to be impossible to reproduce the final fragment distributions by using the ICF model coupled to GEMINI. This suggests that the most-proton-rich fragments result from collisions that are not described within this model.

### 3. Boltzmann-Nordheim-Vlasov calculation

A second, somewhat different calculation was also compared to the data. A Boltzmann-Nordheim-Vlasov (BNV) model [63,64] was used to simulate the dynamics of the reaction. Prediction of the detectable products from the BNV model involves two stages that are similar to the stages in the ICF calculation. The first stage is the dynamic stage of the collision. The second stage is the statistical decay of the excited fragments produced in the first stage. (For clarity during this discussion, "BNV model" refers only to the BNV model of the first stage, while "BNV calculation" refers to the result of coupling the BNV model to the statistical decay model.)

The dynamical stage of the collision was simulated by solving the BNV equation with the test particle approach in a "full ensemble" method (each nucleon being represented by 50 test particles), the self-consistent mean field potential and a nuclear potential approximated by a density-dependent Skyrme-like interaction. The parameters of the latter potential were chosen to reproduce nuclear matter saturation properties and a compressibility coefficient of $K=200$ MeV. The free nucleon-nucleon cross section was used in the collision term with its energy and angular dependence. These are the same values used to reproduce $^{139}$La + Al data at the somewhat higher energy of 55 MeV/nucleon. The collision is followed as a function of time until the slope of the mean kinetic energy of the emitted nucleons versus time curve has changed. This sudden change of the slope is taken to indicate the transition from preequilibrium emission to evaporation from an equilibrated source. At the relaxation time (about 110 fm/c), where the slope of the emitted nucleons' mean energy versus time curve changes, a clustering procedure is used to calculate the $Z$, $A$, $E^*$, and $J$ of each fragment. This procedure forms clusters from the test particles that satisfy the condition $|r_i - r_j| < D$, where $r_i$ and $r_j$ are the positions of the $i$th and $j$th test particles. $D$ is set to the minimum value that allows the clustering procedure to reproduce the target and projectile masses at the start of the calculation ($D = 1.5$ fm). The angular momentum of the cluster is determined by summing the angular momentum of each particle:

$$J = \sum \mathbf{r}_i \times \mathbf{p}_i \qquad (13)$$

in the cluster center of mass. The cluster excitation energy is

$$E^* = E_{\mathrm{kin}} + E_{\mathrm{NMF}} + E_{\mathrm{Coul}} - E_{\mathrm{g.s.}}, \qquad (14)$$

where $E_{\mathrm{kin}}$ is the total kinetic energy, $E_{\mathrm{NMF}}$ is the nuclear mean field energy, $E_{\mathrm{Coul}}$ is the Coulomb energy, and $E_{\mathrm{g.s.}}$ is the ground state total energy calculated from the static solution used as the initial condition for the BNV calculation. The $Z$, $A$, $E^*$, and $J$ of the excited primary fragments at the relaxation time are then used as input values for a statistical decay code (in this case, GEMINI) to simulate the deexcitation process. This calculation is carried out for the entire range of impact parameters. The results for all the impact parameters are combined to give a prediction of the entire reaction.
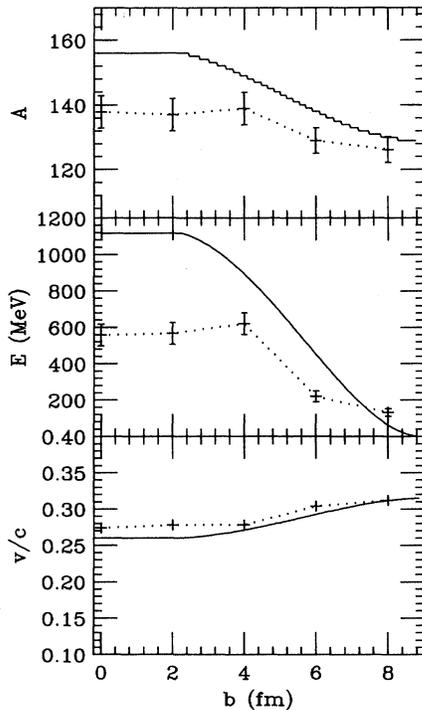
FIG. 23. The mass, excitation energy, and velocity of the primary projectile like fragment as a function of impact parameter from both the BNV (dotted curve) and ICF (solid curve) models for the reaction of 50 MeV/nucleon $^{129}$Xe + Al. The crosses with error bars are the results and uncertainties from the BNV calculation at each impact parameter.

In practice, the clustering procedure sometimes gave incorrect results at the relaxation time, because the primary fragments were not well separated. Fragments that were only slightly separated were frequently clustered together. To overcome this problem, the BNV calculation was extended to longer times (130 fm/$c$) where the clusters were clearly defined. The clusters' $Z$, $A$, $E^*$, and $J$ were determined as a function of time. The functions for $Z$, $A$, $E^*$, and $J$ were extrapolated back to the relaxation time to obtain the $Z$, $A$, $E^*$, and $J$ of the separated fragments at the relaxation time.

The BNV model produces one primary fragment for central collisions at 26–50 MeV/nucleon and two primary fragments for very peripheral collisions at 40 and 50 MeV/ nucleon. Figure 23 shows a comparison of the calculated values for the mass, excitation energy, and velocity of the primary projectilelike fragments from both the BNV and the ICF models for the 50 MeV/nucleon $^{129}$Xe + Al reaction. The crosses with the error bars represent the results and the uncertainties from the BNV model at each impact parameter. The uncertainty in the BNV result arises primarily from determining the relaxation time. The error bars represent variation of the relaxation time by $\pm 5$ fm/$c$. The BNV model predicts smaller masses and excitation energies than the ICF model because preequilibrium emission is allowed in the former and not in the latter. The shapes of the velocity, mass, and excitation energy distributions for the primary projectile-like fragments, however, are very similar for both models

(see Fig. 23). This similarity is seen for all the 40 and 50 MeV/nucleon $^{129}$Xe + Be, C, and Al reactions.

The BNV model predicted the formation of very elongated, rotating objects at 26 MeV/nucleon and large impact parameters. Even at times greater than 300 fm/$c$, the shape did not relax. Since the shape of the primary fragment had not relaxed by this time, the model result was not consistent with the assumption of equilibration within the model's usable time scale. In addition, the excitation energies for all impact parameters at 26 MeV/nucleon became negative between 160 fm/$c$ and 220 fm/$c$ after the start of the collision because of violation of the Pauli principle in the BNV model. The slope of the emitted nucleons' mean kinetic energy curve did not change until 120–130 fm/$c$. This required that the BNV model be run for longer times than it was for the 40 and 50 MeV/nucleon reactions. The longer time requirement, combined with the lower bombarding energy and increased overlap of the Fermi spheres, means that the Pauli-blocking violation is large. Therefore, the BNV calculations were not run for the 26 MeV/nucleon reactions. It should be noted here that the statistical decay calculations assume that shape equilibration has occurred within the time scale of the BNV calculation. For the 40 and 50 MeV/nucleon reactions, the shape of the nuclei at the end of the BNV calculation is approximately spherical. Thus the assumption of shape relaxation may be valid for these reactions. This is clearly not the case for the 26 MeV/nucleon calculations.

Overall, the BNV model produced an incomplete fusionlike reaction (i.e., the projectile nucleus picked up mass from the smaller target nucleus). The excited primary fragments from the BNV model were coupled to a statistical decay model to determine the final fragments. The results of these coupled model calculations are shown in Fig. 24 for the 50 MeV/nucleon $^{129}$Xe + Al reaction. Also shown in Fig. 24 are the predictions from the ICF calculation and the experimental data. The predicted $Z$ value versus velocity distributions and elemental cross sections from the BNV + GEMINI calculations are very similar to those from the ICF + GEMINI calculations. Both models give similar results for the average mass for each element, the width of the mass distribution for each element, and the momentum distributions for each isotope for all the 40 and 50 MeV/nucleon reactions studied. Since GEMINI was used to calculate the deexcitation stage, the BNV + GEMINI calculations also overestimate the average mass for each element and underestimate both the width of the $Z$ distribution as a function of velocity and the width of the isotope distribution for each element. The cause of and solutions to these differences are discussed in detail in Sec. IV B 2.

In general, the differences between the ICF and BNV predictions are small; however, there is one significant difference. The ICF model predicts the production of a target remnant over a large range of impact parameters, whereas the BNV model predicts the production of a target remnant for only very peripheral reactions. For more central collisions ($b$ = 4 fm), where the ICF model predicts a target remnant, the BNV model predicts that the mass not in the primary fragment is left in a few very small fragments ($Z \leq 2$) and many single nucleons. The present experiment is capable of detecting neither the targetlike remnant nor a large number of
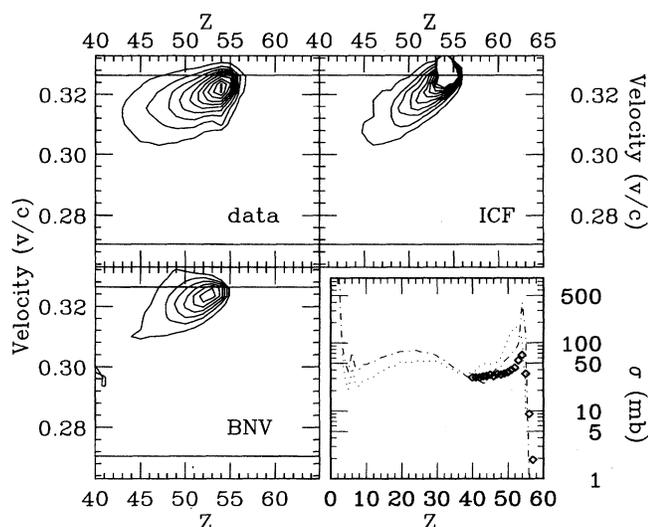
FIG. 24. The upper left frame shows the cross sections in the $Z$ versus velocity plane from the 50 MeV/nucleon $^{129}$Xe + Al reaction. The upper horizontal line corresponds to the velocity of the beam. The lower horizontal line corresponds to the velocity of the center of mass. The upper right frame shows the same distribution predicted by the ICF calculation. The lower left frame shows the distribution predicted by the BNV calculation. The contour lines are linearly spaced. The lower right frame shows the elemental cross sections. The heavy residue cross sections from the current work are shown as diamonds, the ICF predictions as a dashed line, and the BNV predictions as a dotted line.

single nucleons and thus cannot distinguish between the ICF and the BNV model predictions.

The answers to the first two questions that were posed at the beginning of Sec. IX are now clear. It has been shown that heavy residues are produced in complete and incomplete fusion reactions. Models of these reaction mechanisms have predicted the complex fragment data well. These models also predict many aspects (e.g., the elemental cross sections, the cross sections as a function of $Z$ value and velocity, and isotopically resolved momentum distributions) of the heavy residue data reasonably well. The exception to this is that both models predict a less than 50 nb production cross section for the very-proton-rich nuclei but they are observed to have much larger cross sections. These models are able to reproduce the proton-rich nuclei only if currently accepted input parameters of the statistical decay calculation are strongly varied; however, these large variations are not physically justifiable. This suggests that the source of these extremely-proton-rich nuclei must be a reaction that produces cold proton-rich nuclei. The details of this reaction mechanism are not understood within either model examined here.

## V. CONCLUSIONS

The production cross sections of the residues with $Z >$ 39, as a function of $Z$, $A$, and momentum, from the 26, 40, and 50 MeV/nucleon $^{129}$Xe + Be, C, and Al reactions were measured by using a magnetic spectrometer. Combining the

present and previous data, experimental cross sections spanning almost the entire range of $Z$ values produced in these reactions have now been measured. The current data have been compared to those from previous works utilizing similar reactions. Although the elemental cross sections do not overlap previous measurements, they are consistent within experimental errors.

Measurements of the isotopic cross sections by $\gamma$-ray spectroscopy have assumed a smoothly varying cross section distribution to extract the cross sections for the undetectable isotopes. The need for this premise results from the inability of $\gamma$-ray spectroscopy to detect short-lived isotopes ($t_{1/2} < 5$ min). The symmetry of the experimental isotopic cross sections (Fig. 8) for each element and the smooth variation between elements confirm the validity of this assumption.

The experimental $Z$ value versus velocity distributions are consistent with the $Z_{total}$ versus $v_{source}$ distributions determined from complex fragment coincidence data. This study provides a determination of the relative amounts of incomplete and complete fusion that are complementary to that implied in studies of complex fragments. Events with very low excitation energies are easily detected in the present work, since no fissionlike decay is required. These distributions provide strong evidence for an incomplete fusion reaction mechanism.

Many features of the current data were reproduced by an incomplete fusion (ICF) model coupled to a statistical decay calculation. This calculation was able to reproduce the shapes of the heavy residue elemental cross sections and the $Z$ value versus velocity distributions. The complex fragment emission velocities and cross sections from the 40 and 50 MeV/nucleon La + C reactions and the 26 MeV/nucleon Xe + C and Al reactions were well reproduced. The ICF calculation also predicted the independence from the entrance channel of the average mass for each element. The primary failures of this model are its overestimation of the average mass for each element and its underestimation of the widths of the $Z$ distributions as a function of velocity and of the isotope distribution for each element. The momentum distributions provide a new test of the reaction model. The most-proton-rich nuclei are predicted to have a less than 50 nb production cross section and thus the models produced no momentum distribution. The average mass isotope for each element typically has its momentum distribution well predicted by the model calculation. The heavier isotopes of each element are not as well predicted, as the predicted centroid values are too large. The difference between the experimental and the predicted average isotope for each element can be eliminated by small, but systematic, variation of the input parameters for the statistical decay calculation. The width of the $Z$ distribution as a function of velocity and the width of the isotope distribution for each element cannot be reproduced with reasonable input parameters for the calculation.

A Boltzmann-Nordheim-Vlasov (BNV) model coupled to a statistical decay model yields essentially the same prediction as the ICF model for the heavy residue data from the 40 and 50 MeV/nucleon $^{129}$Xe + Be, C, and Al reactions. Both models predict that the heavy residues produced in this energy region result from incomplete fusionlike reactions (i.e., the projectile nucleus picked up mass from the smaller target nucleus). Neither model is able to quantitatively reproduce

the data even with variation of the input parameters over the physically possible range.

The very-proton-rich nuclei detected in the present study are predicted to have a less than 50 nb production cross section by both models. The production mechanism for these very-proton-rich nuclei, as well as the mechanism producing the extremely-proton-rich nuclei observed recently, is not understood within the reaction mechanisms studied here. The models can predict the production of these proton-rich nuclei only if the statistical model input parameters are varied beyond the physically reasonable range.

[1] E.K. Hyde, G.W. Butler, and A.M. Poskanzer, Phys. Rev. C **4**, 1759 (1971).

[2] A.M. Poskanzer, G.W. Butler, and E.K. Hyde, Phys. Rev. C **3**, 882 (1971).

[3] R.G. Korteling, C.R. Toren, and E.K. Hyde, Phys. Rev. C **7**, 1611 (1973).

[4] A.M. Zebelman, A.M. Poskanzer, J.D. Bowman, R.G. Sextro, and V.E. Viola, Phys. Rev. C **11**, 1280 (1975).

[5] J. Gosset, H.H. Gutbrod, W.G. Mayer, A.M. Poskanzer, A. Sandoval, R. Stock, and G.D. Westfall, Phys. Rev. C **16**, 629 (1977).

[6] W.G. Meyer, H.H. Gutbrod, C. Lukner, and A. Sandoval, Phys. Rev. C **22**, 179 (1980).

[7] C. Chitwood, D.J. Fields, C.K. Gelbke, W.G. Lynch, A.D. Panagiotou, M.B. Tsang, H. Utsunomiya, and W.A. Freidman, Phys. Lett. **131B**, 289 (1983).

[8] B.V. Jacak, G.D. Westfall, C.K. Gelbke, L.H. Harwood, W.G. Lynch, D.K. Scott, H. Stoker, M.B. Tsang, and T.J.M. Symons, Phys. Rev. Lett. **51**, 1846 (1983).

[9] L.G. Sobotka, M.L. Padgett, G.J. Wozniak, G. Guarino, A.J. Pacheco, L.G. Moretto, Y. Chan, R.G. Stokstad, I. Tserruya, and S. Wald, Phys. Rev. Lett. **51**, 2187 (1983).

[10] D.J. Fields, W.G. Lynch, C.B. Chitwood, C.K. Gelbke, M.B. Tsang, H. Utsunomiya, and J. Aichelin, Phys. Rev. C **30**, 1912 (1984).

[11] L.G. Sobotka, M.A. McMahan, R.J. McDonald, C. Signarbieux, G.J. Wozniak, M.L. Padgett, J.H. Gu, Z.H. Liu, Z.Q. Yao, and L.G. Moretto, Phys. Rev. Lett. **53**, 2004 (1984).

[12] M.A. McMahan, L.G. Moretto, M.L. Padgett, G.J. Wozniak, L.G. Sobotka, and M.G. Mustafa, Phys. Rev. Lett. **54**, 1995 (1985).

[13] F. Auger, B. Berthier, A. Cunsolo, A. Foti, W. Mittig, J.M. Pascaud, E. Plagnol, J. Quebert, and J.P. Wieleczko, Phys. Rev. C **35**, 190 (1987).

[14] M. Fatyga *et al.*, Phys. Rev. Lett. **58**, 2527 (1987).

[15] B. Borderie, M. Montoya, M.F. Rivet, D. Jouan, C. Cabot, H. Fuchs, D. Gardes, H. Gauvin, D. Jacquet, and F. Monnet, Phys. Lett. B **205**, 26 (1988).

[16] R. Bougault *et al.*, Nucl. Phys. **A488**, 255c (1988).

[17] R.J. Charity *et al.*, Nucl. Phys. **A483**, 371 (1988).

[18] R.J. Charity, D.R. Bowman, Z.H. Liu, R.J. McDonald, M.A. McMahan, G.J. Wozniak, L.G. Moretto, S. Bradley, W.L. Kehoe, and A.C. Mignerey, Nucl. Phys. **A476**, 516 (1988).

[19] L.G. Moretto and G.J. Wozniak, Prog. Part. Nucl. Phys. **21**, 401 (1988), and references therein.

[20] M.F. Rivet, B. Borderie, C. Gregoire, D. Jouan, and B. Remaud, Phys. Lett. B **215**, 55 (1988).

[21] N. Colonna *et al.*, Phys. Rev. Lett. **62**, 1833 (1989).

[22] D.E. Fields *et al.*, Phys. Lett. B **220**, 356 (1989).

[23] H.Y. Han, K.X. Jing, E. Plagnol, D.R. Bowman, R.J. Charity, L. Vinet, G.J. Wozniak, and L.G. Moretto, Nucl. Phys. **A492**, 138 (1989).

[24] R.J. Charity *et al.*, Nucl. Phys. **A511**, 59 (1990).

[25] Y. Blumenfeld *et al.*, Phys. Rev. Lett. **66**, 576 (1991).

[26] D.R. Bowman *et al.*, Nucl. Phys. **A523**, 386 (1991).

[27] D.R. Bowman *et al.*, Phys. Rev Lett. **67**, 1527 (1991).

[28] Y.H. Chung, S.Y. Cho, and N.T. Porile, Nucl. Phys. **A533**, 170 (1991).

[29] D.N. Delis *et al.*, Nucl. Phys. **A534**, 403 (1991).

[30] R.T. de Souza *et al.*, Phys. Lett. B **268**, 6 (1991).

[31] T. Ethvignot *et al.*, Phys. Rev. C **43**, R2035 (1991).

[32] Y.D. Kim *et al.*, Phys. Rev. Lett. **67**, 14 (1991).

[33] E. Plasecki *et al.*, Phys. Rev. Lett. **66**, 1291 (1991).

[34] J.L. Wile *et al.*, Phys. Lett. B **264**, 26 (1991).

[35] J.L. Wile *et al.*, Phys. Rev. C **45**, 2300 (1992).

[36] P. Roussel-Chomaz *et al.*, Nucl. Phys. **A551**, 508 (1993).

[37] J. Feng *et al.*, Phys. Rev. C **50**, 2420 (1994).

[38] D.R. Bowman, Ph.D. thesis, University of California at Berkeley, Lawrence Berkeley Laboratory Report No. LBL-27691, 1989.

[39] K. Hanold, L.G. Moretto, G.F. Peaslee, G.J. Wozniak, D.R. Bowman, M.F. Mohar, and D.J. Morrissey, Phys. Rev. C **48**, 723 (1993).

[40] W.L. Kehoe, Ph.D. thesis, University of Maryland, Report No. DOE/ER/40321-5, 1989.

[41] B.M. Sherrill, W. Benenson, D. Mikolas, D.J. Morrissey, J.A. Nolen, Jr., and J.A. Winger, Nucl. Instrum. Methods B **56/57**, 1106 (1991).

[42] M.F. Mohar *et al.*, Phys. Rev. Lett. **66**, 1571 (1991).

[43] D. Bazin *et al.*, Nucl. Phys. **A515**, 349 (1990).

[44] D.J. Vieira, G.W. Butler, J.M. Wouters, and D.S. Brenner, Annual Report Progress at LAMPF, 1984, p. 192.

[45] M.A. McMahan *et al.*, Nucl. Instrum. Methods A **253**, 1 (1986).

[46] F. Hubert, A. Fleury, R. Bimbot, and D. Gardes, Ann. Phys. (Paris) **5**, 1 (1980).

[47] N.A. Orr *et al.*, Phys. Rev. Lett. **69**, 2050 (1992).

[48] B.M. Sherrill (unpublished).

[49] K.A. Hanold, Ph.D. thesis, University of California at Berkeley, Lawrence Berkeley Laboratory Report No. LBL-36087, 1994.

[50] S.J. Yennello, J.A. Winger, T. Antaya, W. Benenson, M.F. Mohar, D.J. Morrissey, N.A. Orr, and B.M. Sherrill, Phys. Rev. C **46**, 2620 (1992).

[51] A. Lleres, Ph.D. thesis, L'University Scientifique Technologique et Medicale de Grenoble, 1988.

[52] J.A. Winger *et al.*, Phys. Rev. C **48**, 3097 (1993).

[53] D.J. Morrissey (unpublished).

[54] M. Lewitowicz *et al.*, Nouv. GANIL **48**, 7 (1993).

[55] G.F. Peaslee (unpublished).

[56] M. Colonna, P. Roussel-Chomaz, N. Colonna, M. Di Toro, L.G. Moretto, and G.J. Wozniak, Phys. Lett. B **283**, 180 (1992).

[57] M. Colonna, M. Di Toro, V. Lataora, and N. Colonna, Nucl.

[58] D.R. Bowman *et al.*, Phys. Rev. C **46**, 1824 (1992).

[59] H. Hauser and H. Feshbach, Phys. Rev. **87**, 336 (1952).

[60] L.G. Moretto, Nucl. Phys. **A247**, 211 (1975).

[61] L. Tassan-Got (private communication).

[62] P. Möller and J.R. Nix, Nucl. Phys. **A361**, 117 (1981).

[63] A. Bonasera, G.F. Burgio, and M. DiToro, Phys. Lett. B **221**, 233 (1989).

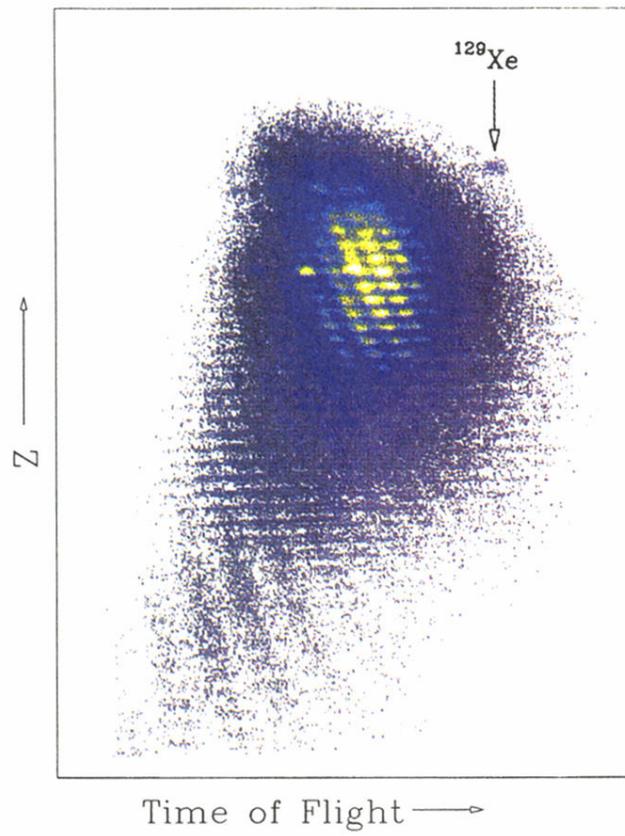[64] A. Bonasera, G. Russo, and H.H. Wolter, Phys. Lett. B **246**, 337 (1990).

Phys. **A545**, 111 (1992); **A541**, 295 (1992).

FIG. 2. Measured $Z$ versus time of flight for the 50 MeV/nucleon $^{129}$Xe + Al reaction.